University of Wollongong

Research Online

University of Wollongong Thesis Collection 2017+

University of Wollongong Thesis Collections

2019

Hystent Project: 3D-printed cardiovascular stents. Customization of 3D printer and development of stents

Diego Castaneda Garay

Follow this and additional works at: https://ro.uow.edu.au/theses1

University of Wollongong

Copyright Warning

You may print or download ONE copy of this document for the purpose of your own research or study. The University does not authorise you to copy, communicate or otherwise make available electronically to any other person any copyright material contained on this site.

You are reminded of the following: This work is copyright. Apart from any use permitted under the Copyright Act 1968, no part of this work may be reproduced by any process, nor may any other exclusive right be exercised, without the permission of the author. Copyright owners are entitled to take legal action against persons who infringe their copyright. A reproduction of material that is protected by copyright may be a copyright infringement. A court may impose penalties and award damages in relation to offences and infringements relating to copyright material. Higher penalties may apply, and higher damages may be awarded, for offences and infringements involving the conversion of material into digital or electronic form.

Unless otherwise indicated, the views expressed in this thesis are those of the author and do not necessarily represent the views of the University of Wollongong.

Research Online is the open access institutional repository for the University of Wollongong. For further information contact the UOW Library: research-pubs@uow.edu.au

Universiteit Utrecht

UNIVERSITY OF WOLLONGONG AUSTRALIA

Hystent Project:

3D-printed cardiovascular stents
Customization of 3D printer and development of stents

by
Diego Castaneda Garay, MD

Supervisors:
Gordon Wallace, AO; Stephen Beirne, Ph.D.; Sepidar Sayyar, Ph.D.
Co-supervisor: Zhilian Yue, Ph.D.

This thesis is presented as part of the requirements for the conferral of the degree:

Biofabrication

Utrecht University; Graduate School of Life Sciences.
UU student number: 5807646

University of Wollongong; School of Medicine, Science and Health
UoW student number: 5914097
November 2019

Certification

I, Diego Castañeda Garay, declare that this thesis is submitted in fulfillment of the requirements for the conferral of the degree Biofabrication, from the Utrecht University and the University of Wollongong, is wholly my own work unless otherwise referenced or acknowledged. This document has not been submitted for qualifications at any other academic institution.

_____

Diego Castañeda Garay

November 2019

Acknowledgments

I want to thank my supervisors Gordon, Stephen, Sepidar and Zhilian, their patience and dedication to my project was priceless. Also, I want to recognize Grant Barnsley, Ashley Walker, Cameron Angus, Holly Warren, Rhys Cornock, Tony Romeo, Mitchell Nancarrow, and Patricia Hayes for their selfless support on my mischiefs at IPRI.

To the Darrel Boyz, they stood up with me during this whole project: Jeremias, Malaquias, Stefano, Gilberto, Maximiliano, and Gregorio.

To my family, they always support me on this Biofabrication journey.

To my wife. She is the world to me. Without her, none of this would ever happen.

Abstract

Bioresorbable stents promised the restoration of the coronary blood flow without the long-term complications of their non-resorbable counterparts. Although maintaining coronaries open using bioresorbable stents for prolonged periods has proven challenging, using biodegradable polymeric composite materials could potentially solve this issue. To fabricate these polymeric structures, additive manufacturing may provide an accessible and customizable platform. This research examines the development of a novel customized dual-printhead bioprinter that was utilised for 3D printing polymer-based stents incorporating graphene composites.

The customized bioprinter was used to 3D print stents from polycaprolactone (PCL) and PCL graphene-based composites. Graphene oxide (GO) and edge functionalized graphene (EFG) were used as fillers to develop appropriate composites for fabrication of single- or hybrid-material architectures.

Single-material stents fabricated using PCL/EFG composites outperformed PCL/GO 1% and blank PCL stents. PCL/EFG 1% stents showed an increased radial strength by 27% and tensile strength by 23% compared to blank PCL stents. PCL/EFG 5% stents showed higher radial strength by 36% compared to blank PCL stents. Hybrid material stents using PCL and PCL/EFG 1% were subjected to mechanical property testing, degradation tests and used as a drug-delivery platform. Hybrid-material stents compressive and tensile strength were inferior compared to single-material stents, which might be improved through further optimization.

Enzymatically degraded hybrid stents were found to be bioresorbable with a rate slower than previously reported for PCL. Drug delivery capabilities of hybrid stents were studied using paclitaxel-loaded stents. Hybrid stents showed a slower cumulative drug release by 36% against blank PCL stents.

These results demonstrated the feasibility of a stent bioprinter and the improvement of mechanical properties with the use of EFG composites while preserving bioresorbable and drug-delivery capabilities.

Disclaimer

This research was funded by the *Consejo Nacional de Ciencia y Tecnología*, through the Scholarship for *Estudios de postgrado en el extranjero*. Universidad de Guadalajara contributed with a complementary scholarship through their program *Becas para inicio o continuación de estudios de postgrado en el extranjero*.

Table of contents

I. List of abbreviations

BMS	Bare-metal stents
BRS	Bioresorbable stents
CVD	Cardiovascular disease
DES	Drug-eluting stents
DFC	Dynamic feedrate compensation
DSC	Differential scanning calorimetry
EFG	Edge-functionalized graphene
FDM	Fused deposition modeling
GO	Graphene-oxide
HMS	Hybrid-material stents
LST	Late stent thrombosis
LVSEM	Low Vacuum Scanning Electron Microscope
MEW	Melt electrospinning writing
mTOR	Mammalian target of rapamycin
PAGA	Polyacetyglutamic acid
PBS	Phosphate buffer saline
PCI	Percutaneous coronary intervention
PCL	Polycaprolactone
Pcx	Paclitaxel
PDX	Polydioxanone
PLGA	Polyglycolic acid/polylactic acid
PH	Printing head
PLA	Polylactide acid
POE	Polyorthoesters
SEM	Scanning electron microscopy
SMS	Single-material stents
TEA	Triethylamine
TGA	Thermogravimetric analysis

II. List of figures

III. List of tables

Aims

The work presented here aims to construct a customized printer capable of fabricating hybrid PCL and graphene-based composite stents then characterize stent mechanical properties, drug delivery capabilities, and degradation profile. To achieve these goals the work was divided into the following two segments.

1. Customization of an existing bioprinter into a dual-printhead stent fabrication system
    a. Hardware:
        i. Design and implementation of a rotary axis with angular control with a user-friendly manually secured mandrel.
        ii. Optimization of hybrid-material printing and temperature control
    b. Software:
        i. Development of a G-code generator software for hybrid-material 3D-printed stents
2. Fabrication of hybrid-material 3D-printed stents and characterization of mechanical properties, degradation kinetics, and drug-eluting capabilities
    a. Development and characterization of PCL/graphene composites
    b. Fabrication of hybrid-material stents using PCL and PCL/graphene-based composites

1. Introduction

In Australia, cardiovascular disease (CVD) is a major cause of death with 43,963 deaths attributed to it in 2016 [1]. CVD is one of the major burdens in health and economy for Australia, affecting one in six Australians and resulting in one death every 12 minutes [1,2]. Similar statistics are present in the US where CVD is projected to cost $276 billion/annum in 2030 [3]. CVD is a heart injury that result as a consequence of several diseases characterized by decreased blood flow in the coronary arteries [4]. While there are many treatments for CVD, the most common is percutaneous coronary intervention [5,6]. The percutaneous coronary intervention aims to restore the blood flow by opening a blocked coronary artery and deploying a cardiovascular stent to help keep the artery open.

1.1. Bioresorbable stents

Stents are tubular structures that can be made from different materials, in a wide range of architectures via several manufacturing methods [7]. Most of the commercially-available stents are composed of a metallic structure that can be produced using laser micro-cutting, waterjet-cutting, photo-etching and wire-forming [7]. Overall, stents can be classified in two generations. The first-generation stents are bare-metal stents (BMS). A BMS was implanted for the first time in 1986 and improved the clinical outcome of CVD dramatically [5,8]. However, complications of restenosis occur in 20-30% of patients, along with other less common late complications including in-stent thrombosis and coronary intimal hyperplasia [9,10]. The second generation is drug-eluting stents (DES) that emerged to reduce BMS complications. DES are metallic stents coated with a drug-eluting layer and are the most common type of stents used worldwide. These stents represent a major technological step forward in the treatment of CVD [11]. DES presented different kinds of complications, such as late stent thrombosis (LST) and self-perpetuating inflammation, both a major concern for clinicians [12,13]. The risk of these complications increases 6 months after deployment, once the coronary healing process is complete [8,12].

To tackle DES related complications, a new kind of stent was developed, bioresorbable drug-eluting stents (BRS). BRS aims to restore the blood flow and once the healing process is complete, being degraded and reabsorbed [14]. BRS can be made of bioresorbable metals, polymers or a combination of both. BRS can be fabricated using polymers such as polylactide acid (PLA), poly-L/D-lactic acid (PLLA/PDLA), polydioxanone (PDX), polycaprolactone

(PCL), polyglycolic acid/polylactic acid (PLGA), polyacetyglutamic acid (PAGA), and polyorthoesters (POE) [14,15]. It has been suggested that mechanical support is needed to counteract negative remodeling and restenosis between one and three months. After 6 months the stent presence could be disadvantageous and lead to increasing the risk of late stent thrombosis [8,12,16,17]. Due to its bioresorbable nature, BRS allow artery healing and remodeling, without the long-term presence of foreign material.

1.2. Additive manufacturing of bioresorbable stents

Polymer-based BRS have created a converging point for enhanced composite materials and novel manufacturing technologies. One of these manufacturing techniques is fused deposition modeling (FDM). FDM is an additive manufacturing technique that uses melted polymers to print a physical object in a layer-by-layer fashion, based on a computational model [18]. The melted polymer is deposited using a printing head (PH) that moves in a three-dimensional space, using a three-axis coordinate system (X, Y, and Z). The melted polymer is deposited onto a flat build plate that can be passively or actively heated. FDM technology has been used for stent fabrication with two different approaches. One is based on printing onto a rotary-axis and the second uses a flat build plate with post-processing to curve the print into a cylindrical shape [19,20]. Both proposed printers are limited to single nozzle setups [20]. Other additive technologies have been used to manufacture cylindrical scaffolds. Melt electrospinning writing (MEW) was used to produce cylindrical scaffolds with two types of rotary stages, a speed-controlled stage [21] and a code controlled rotary axis [22]. MEW produces nanometer dimensional struts with high-precision multilayer deposition and dimensional control. These type of cylindrical shapes offers a significant surface to volume ratio, ideal for drug-delivery, although these constructs showed low mechanical strength and the incorporation of drug-loaded polymers changes drastically the printer parameters, even one of those printers rely on coagulation baths after printing exposing the stents to organic solvents [21]. Stereolithography was also used for stent fabrication with the limitation of using cytotoxic resins not feasible for biological applications [23]. To the best of this author's knowledge, no dual print head (dual-PH) rotary-axis printer for stent fabrication has been previously reported. A dual-PH printer, similar to the one proposed in this work, expands the range of fabricated architectures and enables the fabrication of hybrid-material 3D printed BRS with post-processing.

The movement of the PH in an FDM printer runs along their axis that can be linear, angular or a combination of both. The developed 3D printing solution uses a linear motion over a rotary-axis for stent fabrication, combining linear movements with angular rotation. Printer movements are directed based on standard G-code. G-code is a language that translates the intended design into a precise stepwise printer mechanical motion. To obtain these instructions a stent G-code generator is needed. Recently, a G-code generator software was proposed to print cylindrical scaffolds to melt-electrospinning writing [22]. This software produces a proprietary type of G-code, not compatible with generic printing systems. Also, this code is intended to solve specific issues that exist in the melt-electrospinning writing process, with are not factor in the FDM systems. Other reported stent printers do not specify how the G-code is generated for their stents [19,20]. As an essential part of this research, a G-code generator for stent printing that uses basic parameters for three different architectures is described.

The use of additive manufacturing to fabricate stents can be a paradigm shift in the clinical setting. Currently, stents are produced in large quantities with a handful of architectural configurations available; however, the production process from the raw material up to hospital deployment can take up to 150 days [7,24]. Efforts have been made to produce on-demand stents by using additive manufacturing technologies [20,24–26]. However, all of them require a post-processing step that can lead to structural damage and inadvertently to a failed intervention. There is a need for manufacturing capabilities that can be widely adopted without additional post-processing. A one-click solution to produce stents at the bedside would put in the hands of clinicians the tools to swiftly obtain life-saving devices that otherwise would have to be made by elsewhere [27].

1.3. Graphene-based composites for stent fabrication

Currently, there are few commercially available BRS, all of which have seen limited success and one which has been discontinued in the past year [28,29]. One of the main issues with BRS is their insufficient mechanical properties, as bioresorbable polymers are weaker than their metallic counterparts [9,15]. In an effort to improve the mechanical properties, bioresorbable composites have been developed to draw on the benefits of both materials. Some of these composites use bioresorbable polymer with a nanofiller, such as graphene, calcium phosphate and hydroxyapatite [30–32]. Of the several types of graphene-based nanofillers, graphene-oxide (GO) and edge-

functionalized graphene (EFG) were selected as test composites in this research. GO is a known biocompatible nanofiller capable of increasing PCL mechanical properties [31]. EFG is a novel graphene-based nanofiller currently in development by the Intelligent Polymer Research Institute at the University of Wollongong, Australia, and for this project, a novel PCL / EFG composite was prepared. EFG was obtained by adding functional groups at the edge of the graphene nanosheet, which acts as wedges to prevent nanosheet aggregation. It is expected that EFG nanostructure and properties resemble more to graphene than other graphene-based molecules.

Graphene-based nanofillers have been used to form composites in biomedical applications to enhance polymer properties and capabilities [33]. The incorporation of graphene nanoplatelets can increase the conductivity and mechanical properties of materials [34–36]. Polymer composites made out of graphene-based nanofillers can improve mechanical properties, increase conductivity, increase cytocompatibility, and modified drug-eluting capabilities [19,34–37]. Some studies demonstrate no short-term toxicity and also, antibacterial and antitumoral properties [37,38]. PCL is known to be a biocompatible and bioresorbable polymer with a semi-crystalline structure with wide acceptance in the manufacturing of implantable biomedical devices [39,40]. Besides PCL's compatibility with nanofillers such as graphene-based molecules, PCL can also be used as a drug-eluting carrier [41]. These characteristics made PCL graphene-based composites an ideal test subject to demonstrate the capabilities of the hybrid stent printer (Hystent printer) for stent fabrication in these studies.

1.4. Characterization of bioresorbable stents

Mechanical properties of a stent, such as radial and tensile strength, can modify its safety and efficacy greatly [42,43]. Radial strength of commercially available BMS range from 2.7 to 5.4 N at a 50% strain with a strut thickness range from 156 to 200 µm [16,43,44]. Recently, 3D printed stents were fabricated with a strut thickness as low as 400 µm [20]. Thicker struts increase stent radial strength but increase the thrombogenic risk due to higher flow disturbances [42,45]. There is a need for BRS with thinner struts and composed of enhanced polymers with a radial strength similar to BMS and DES while their degradation rate enables coronary healing while keeping the artery open.

A requirement of modern stents is the sustained release of a pharmacological agents capable of increasing the effectiveness of the stent [46]. Drugs incorporated into stents can be divided, pharmacologically, into antiproliferative and immunosuppressive drugs. For the first group, several drugs have been tested, but only Paclitaxel (Pcx) has demonstrated superior performance and reliability when incorporated onto cardiovascular stents [39,46]. Pcx is a lipophilic cytotoxic molecule with potent antiproliferative activity [46–48]. Pcx has been successfully incorporated into PCL and it has been proved to have an acceptable *in-vitro* release profile [49].

This research thesis is focused on the development of the Hystent printer and characterization of the 3D printed stents and in particular, examining mechanical strength, degradation, and drug-eluting capabilities. The printer has been developed by modifying a commercially available bioprinter with the implementation of a rotary stage. By using the printer and graphene-based composites, SMS were printed, and their mechanical properties characterized. After selecting the composite with the best mechanical properties, HMS's were fabricated and enzymatically degraded to test the bioresorbable profile of graphene-based composites and their mechanical properties during degradation. Finally, Pcx was loaded into HMS to test *in-vitro* drug-release capabilities.

2. Material and methods

2.1. Printer customization

The customized Hystent printer was based on an Inkredible+ (Cellink, Sweden). Marlin Firmware (Marlin firmware. marlinfw.org) was used for printer control.

For material reservoir thermal management optimization, heating elements were relocated closer to the dispensing nozzle. Thermistors were replaced with PIC 100 kΩ generic thermocouples and aligned with the heating elements to accurately monitor material reservoir temperature [50]. Also, heating elements were rewired to the printer board hi-power outputs to improve control and increase maximum temperature. A temperature test was performed with empty printhead (PH) to a maximum temperature of 220 °C. Titanium and aluminum material reservoirs were manufactured using a Realizer SLM-50 metal printer (Realizer GmbH., Germany).

A rotary axis was implemented using a generic NEMA 8 biphasic stepper motor (8HS15-0604S. Osmtec, China). Rotary axis and additional parts of the rotary axis were designed using Solidworks 2017 (*Dassault Systèmes*, S.A., France), prototyped in FDM-printed ABS and the final robust version was printed with nylon-based Onyx filament on a Markforged Mark Two (Markforged Inc., USA). The NEMA 8 stepper motor was wired as an extruder feeder and firmware was set up as a dual-PH single stepper. To accommodate the rotary axis a customized printing platform was implemented along with minor mechanical calibration. The whole set-up was designed as a manually adjustable system, reliable, and user-friendly.

From the factory, the Inkredible+ bioprinter comes with double pneumatic linear actuators to switch and position the active PH. These pneumatic actuators operate unrestricted from the wall pressure, causing a violent change of PH position when switching between active printheads that can cause wear and excessive vibration on the mechanical parts. To manage and dampen this issue inline flow restrictors (AS1002F. RS Components, UK) were installed to control the gas flow rate and in turn the movement speed of the linear actuators.

2.2. G-code generator

The Hystent printer uses standard G-code where every command is designed to order simple actions for the printer. This command can be written by hand or generated via software. In this project, the latter option was

chosen. A G-code generator was build using Microsoft Visual Basic (Microsoft Inc., USA). The G-code generator was planned as the Hystent printer companion to test and develop customized 3D-printed stents. Three stent structure designs were planned, rhomboidal, sinusoidal and continuous sinusoidal. These designs were planned to be customizable with a user-friendly interface.

2.3. Composite preparation

The Hystent printer was planned to develop a bioresorbable HMS. This research aims to move one step closer to clinically relevant stents, thus graphene-based composites were fabricated having in mind this directive. Composite materials were utilized to develop stents with tailorable mechanical properties, drug-eluting capabilities, and degradation. These composites were based on graphene oxide and the new graphene-based nanofiller, EFG. In previous studies [36,51], it has been shown that the addition of graphene-based nanofillers with 1-5 wt% concentration can improve the mechanical and electrical properties of PCL. To examine the effect of EFG-based nanofillers in PCL composites, 1 and 5 wt% concentrations were selected.

2.3.1. GO-based composite

GO was dispersed in PCL at 1 wt.% as previously described [31]. PCL was purchased from Polysciences (Cat. 19561-100, M_W 43KDa. Polysciences Inc. USA) and used as received in pellet form. From the initial aqueous GO dispersion, water was replaced by N,N'-dimethylformamide (DMF) through centrifugation and sonication. PCL was dissolved in the GO-DMF dispersion at 55 °C to obtain a 1 wt.% GO concentration. Homogeneous mixing was ensured by using constant stirring for at least 6 hours followed by ultrasonication for 4 hours at room temperature. A cold isopropanol coagulation bath was used for DMF removal. The coagulated mix was allowed to dry out overnight followed by 3-hours in a vacuum oven at 55 °C. The remaining composite flakes were cut into smaller pieces and washed with ethanol to remove solvent residues followed by overnight evaporation at room temperature.

2.3.2. EFG-based composites

A new graphene-based nanofiller was used in this project, EFG. EFG synthesis and composite preparation cannot be disclosed in this work, EFG is an ongoing project that has not been published yet. EFG will be used in two variants, EFG alone and EFG with triethylamine (EFG TEA). TEA was used to improve EFG dispersibility. Both PCL/EFG and PCL/EFG-TEA were prepared at 1% and 5% in a similar fashion as PCL/GO composite. EFG synthesis and composite preparation was the work of Dr. Ashley Walker.

2.4. Thermogravimetric analysis

To measure thermal stability and nanofiller content, samples were tested using a Q500 Thermogravimetric Analyzer (TGA. TA Instruments, USA). All samples (n=4) were heated up to 600 °C at 10 °C/min in a nitrogen-rich environment. At 600 °C nitrogen was switched to ambient air, to allow oxidative reactions, and heated to 900 °C. Beforehand, the platinum pan was cleaned thoroughly and tared. Changes in weight and temperature were recorded, nanofiller content was measured at 700 °C as described by the manufacturer [52]. Also, degradation temperature and temperature at 10% weight loss were recorded. Results were analyzed with TA Universal Analysis software (TA Instruments, USA).

2.5. Differential scanning calorimetry

Crystallization and melting behavior of graphene-based composites (n=3) were measured using Q10 Differential scanning calorimetry (DSC, TA Instruments, USA). Samples with weights from 5 to 12 mg were contained in aluminum pans, and an empty pan was used as a reference. Melting traces were obtained by heating from room temperature to 200 °C at 10 °C/min. Then samples were cooled to 0 °C to record crystallization temperature. Crystallinity was calculated according to Equation 2.1 [30].

$$\propto = \frac{\boldsymbol{H_{melting}}}{\boldsymbol{H_{\infty}\left(1 - \frac{\%weight\ nanofiller}{100}\right)}} \qquad \text{Equation 2.1}$$

Where α is the degree of crystallinity for nanofiller composites, $H_{melting}$ is the latent heat at melting temperature, H^{∞} is the enthalpy of melting a fully crystallized PCL. Results were analyzed with a TA Universal Analysis software (TA Instruments, USA).

2.6. Rheological properties

To investigate the influence of graphene-based nanofillers on the viscosity of PCL-based composites and their printability potential, rheological properties were recorded using an AR-G2 Rheometer (TA Instruments, USA) using a cone-shaped geometry (angle 2.1°, diameter 55 mm, truncation 55 µm). First, viscosity was measured at steady-state flow under ramped temperature at a constant shear rate (1/s). The temperature was varied from 140 °C to 50 °C, corresponding to the printing temperature and melting point of PCL. Second, viscosity was recorded under a ramped shear rate from 0.001/s to 100/s at a constant 120 °C.

2.7. Stent design and printing settings

Blank PCL and graphene-based composites were extruded using the Hystent printer in pressurized cartridges with 300 µm nozzles. The printing temperature was set at 120 °C with an applied extrusion pressure of 300 kPa, printing speed was set-up between 40 and 60 mm/min to produce round fibers with an average diameter of 275 µm. Printing speed was dynamically decreased by 50% at the joint points to prevent under extrusion zones. The design used for stent printing was rhomboidal with the customized G-code. This is composed of pairs of single lines that form a rhomboidal shape where the length of arms and angle in between those can be controlled. A 6-pair strut was used for single and hybrid-material printing. In HMS, 3 pairs were symmetrically assigned to every material. Stent dimensions for struts were 2.5 mm length, 45° angle, and 4mm inner diameter. The designs and dimensions were chosen to mimic architectures of commercially available bioresorbable stents [15,24] insofar as possible, with the aim of providing a basic model for more complex structures in future projects by using the proposed g-code generator. Stents were printed with strut thickness of 275 µm using a 400 µm nozzle. A lower strut diameter was achieved using a lower diameter nozzle. However, clogging and sample to sample variability increased, especially for GO-based composite and composites with a high EFG nanofiller content.

2.8. Mechanical testing of single- and hybrid-material stents

Mechanical properties of the stents (n=4 per group) were measured using a mechanical tester (EZ-L Shimadzu Corporation, Japan) on samples with 27 mm length and 4 mm ID. For axial measurements, samples were attached to a customized clamp adaptor to avoid prior stent deformation (Appendix A). Stents were adhered to the clamp by using epoxy glue Araldite 5 Minute every day (Selleys Pty., Australia). Care was taken to avoid glue contamination over the stents. Cyclic radial compression and axial compression were conducted for 10 cycles with a 2 mm stroke at 10 mm/min. Tensile tests were performed at 2 mm/min stroke until sample breakage. Attention to clamp alignment was crucial for reliable results. All tests were made in triplicates where the maximum force was recorded, and the average was reported.

Once the mechanical properties of SMS were tested, the stronger composite was selected to fabricate HMS. HMS was printed using blank PCL and the chosen graphene-based composite. HMS mechanical properties were established in the same fashion as for SMS.

2.9. Manufacture of Pcx-loaded composites

Drug-loaded bioresorbable stents used in the clinical practice are loaded upto 90µg of Pcx[46]. Due to Pcx toxicity[47], Pcx-loaded composites were fabricated at 1% (wt/wt) to reduce the risk of exposure to a minimum while mainting a viable drug-release during pilot phase. The polymer was dissolved in methanol at 55 °C under constant stirring in a water bath. Pcx was incorporated, homogeneous mixing was ensured by using constant stirring for at least 3 hours. The mixture was distilled overnight in a water bath at 55 °C using a distillation apparatus with constant rotation. Once the mixture was distilled, the composites were removed and reduced into small pieces for adequate handling. Pcx was loaded into blank PCL and PCL/EFG 1% composite.

2.10. Hybrid-material stents drug-eluting study

To test HMS drug-eluting potential, Pcx was loaded into one of the materials used for stent printing. From the two groups, PCL and EFG groups, samples (n=3 per group) were submerged in a PBS solution with 0.05% Tween-20. The surfactant was used to prevent Pcx precipitation, this was based on the work of Maxim Brodmerkel [53]. Once the stents were submerged in 1 mL of the solution, both groups were incubated by means of a water bath at

37 °C. The first sample was collected at 24 h, with consecutive collections every 48 h. In total, five collections were made. All samples were collected and preserved at -20 °C until measuring. For measuring, samples were thawed at room temperature. Once in liquid form, samples were filtered using 0.22 µm pore hydrophilic PTFE filters (MicroScience, Australia) and deposited into 300 µL HPLC polypropylene vials (J. G. Finneran Assoc., USA). High-performance liquid chromatography (HPLC) was used to estimate the *in-vitro* drug-eluting capabilities of HMS [54]. An LC1260 Infinity II LC system (Agilent Technologies, USA) was employed for the study, using a Zorbax Eclipse Plus C18 column (Agilent Technologies, USA) at 35 °C with UV detection at 230 nm. The mobile phase comprised 55% milliQ water and 45% acetonitrile (CH_3CN). A 1.2 mL/min flow rate and 10 µL injection volume was used. Pcx was integrated at 8.2 min retention time. Control, measurements, and analysis were performed by using the software ChemStation for LC Systems (Agilent Technologies, USA). Details about the standard calibration curve can be found in Appendix E.

2.11. Degradation profile of hybrid-material stents

An enzymatic degradation study was conducted to evaluate the degradation profile of graphene-based HMS. A Lipase type XII from Pseudomonas sp. (Cat. L9518. Sigma-Aldrich, USA) was prepared and used with an activity 8 U/mL in 0.1 M PBS solution [55,56]. HMS samples (n=3) of 10 mm in length were printed and weighed, then submerged in 1.5 mL of the enzyme solution. Immediately after, samples were transferred into a water bath at 37 °C and incubated between 24 and 96 hrs. The enzyme solution was refreshed every 24 h to avoid saturation. After enzymatic degradation, HMS was washed using DI water, dried for at least 24 h, then the dry weight was recorded and compared.

2.12. SEM imaging

Scanning electron microscopy (SEM) images from degraded stents were taken with a Low Vacuum Scanning Electron Microscope (LVSEM) JEOL JSM-6490LV (Jeol, Japan) operating in high vacuum mode. All the samples were coated in 15 nm platinum coating by a Dynavac SC100MS magnetron sputter coating system (Dynavac, USA). Secondary electron imaging was done at 2 kV accelerating voltage, probe current was set at 11 pA and the specimen

set at a working distance of 6.6 mm. Images from degraded stents were obtained before enzymatic degradation, and after 24 h, 48 h and 72 h of enzyme exposure.

2.13. Raman spectroscopy

The spectrograph was obtained by using a LabRam HR 800 Raman Spectrometer (Horiba Scientific, Japan) with a HeNe-laser at the wavelength of 632.81 nm (13.50 mV), the acquisition time of 10 s with a spectrum range of 400–4000 cm^{-1}. Baseline correction was made using LabSpec 6 Spectroscopy Software (Horiba Scientific, Japan).

2.14. Printing drug-eluting hybrid-material stents

To test HMS drug-eluting capabilities, rhomboidal stents composed of 6 pairs of struts were fabricated using the Hystent printer. Stents were fabricated using blank PCL in 3 pairs of struts and a drug-loaded material for the remaining struts. Pcx was loaded into blank PCL (PCL group) and PCL / EFG 1% (EFG group) (n=3 per group). Both Pcx-loaded materials were prepared following the procedures describe in the Section 2.3. Composite preparation. Samples were handled with extra care due to the cytotoxic nature of paclitaxel.

2.15. Statistical analysis

Results were analyzed by the Student-T test and One-way ANOVA with Tukey's post-test with 0.05 significance. Statistical analysis and graphs were plotted using Origin Pro 9.0 (Origin Lap Corp, USA).

3. Results

This research intended to develop a customized stent printer capable of processing materials at temperatures of up to 150 °C with a rotary-axis and heated dual-PH's. A commercially available bioprinter was chosen for the customized system to be based on the existing heated dual-printhead, open-source hardware and firmware. This printer was modified to optimize temperature management, control of interchange of dual-printhead's and implement a G-code controlled rotary axis. The developed platform was then used to fabricate SMS and HMS with PCL and graphene-based composites. SMS and HMS were mechanically tested. HMS was degraded then mechanically tested and drug-eluting capabilities verified.

3.1. Printer customization

From the factory, the bioprinter is equipped with heated dual-PH. Pneumatic actuators and solenoid valves to control PH position and extrusion. Mechanically, the bioprinter is based on a standard CoreXY configuration with open-source generic components. The mainboard consists of a Rambo board 1.3 (Ultimachine., USA). The heating unit was optimized, and a rotary axis implemented.

3.1.1. Heating unit optimization

The machine heating units were upgraded with PIC 100 kΩ NTC 3950 thermistors, stock thermistors were not intended for the high temperatures required for melt extrusion. The control board was rewired to ensure safety and adequate power distribution by using high-power outputs. Out of the box, the printer reached a maximum temperature of 105.0 °C, this can be explained by the biological-oriented design of the bioprinter. The printer was tested to reach the maximum temperature possible before getting thermal runaway errors from the printer. After heating unit optimization, the maximum temperature measured by the printer was 189.5 °C. This configuration provides a more suitable platform for stent printing with PCL-based polymers. Further work must be done to optimize the thermal performance of the aluminum cartridge holder to reduce heat dissipation.

3.1.2. Rotary-axis

To incorporate a rotary-axis a customized printing platform was implemented. The platform was designed having in mind a hands-only approach, reliability, and performance. The design comprises fewer moving parts while maintaining the desired performance (Figure 3.1). The rotary-axis was wired as a PH feeder to take advantage of its native G-code controlled features. The manufacturer provided the stock firmware for the bioprinter, but it proved to have a challenging implementation. Instead, a customized Marlin version was created and flashed into the printer.

The Hystent printer has 106 µm resolution in the X and Y axis, 25 µm Z axis, and 0.12° for the rotary axis. PH can be lowered or raised independently with similar dispensing control. Movement precision can be upscaled by installing high-precision stepper motors and the rotary axis can hold different mandrel diameters with minor changes.

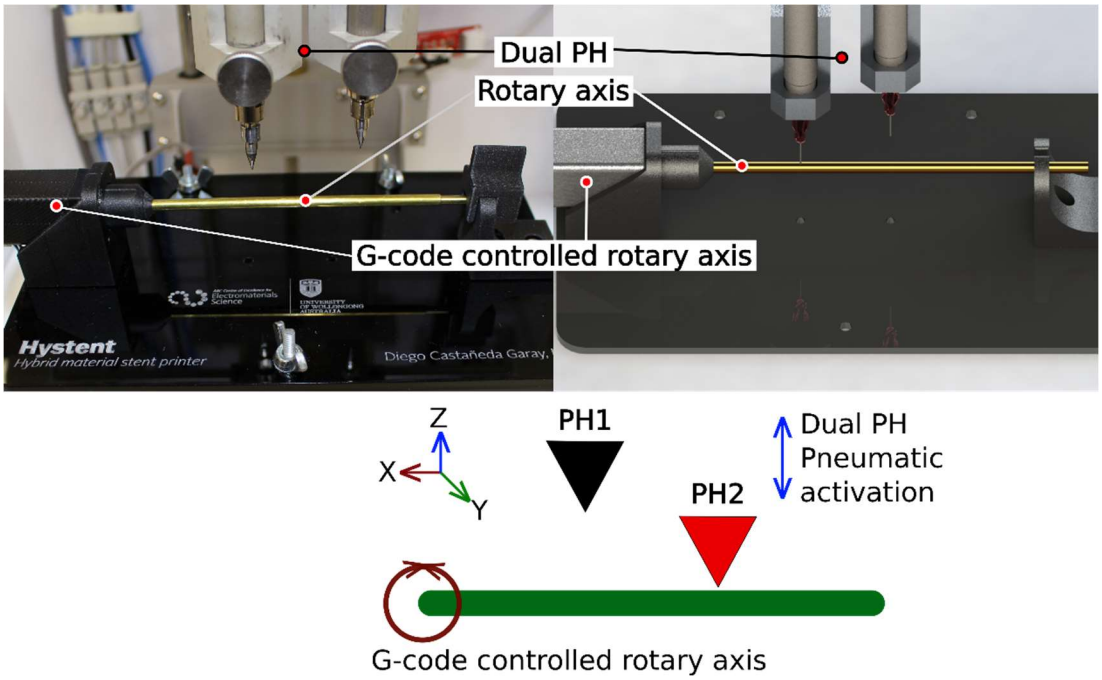

Figure 3.1. Schematic for the Hystent printer. The printer offers standard XYZ 100 µm resolution-movement with the addition of a G-code controlled rotary axis with 0.12° accuracy.

The Hystent printer has independent dispensing control for both PH. This independent control enables the simultaneous printing of two materials with fixed offset capable of handling mixing nozzles. As a part of the

customization, in-house designed and 3D-printed titanium cartridges were created. These cartridges were fitted into the existing PH (Appendix B). Cartridges have a calculated capacity of 1.89 cm^3. Additionally, the cartridges use commercially available M6 Luer tap, M4 pneumatic fittings, and 300 µm stainless steel nozzles.

3.2. G-code generator

To fabricate any structure using AM, a set of instructions must be provided to the printer. For this reason, a G-code generator was developed. This software creates parametric G-code instructions with a user-friendly interface (Figure 3.2). By using simple parameters, a customized set of instructions are produced to feed into the Hystent printer. Thus, allowing optimization of stent architecture with a streamlined G-code generation. Any stent design can be obtained via code. Stent parameters are mandrel diameter, stent length, arms angle, arm length, feedrate and dynamic feedrate compensation (DFC). Currently, the software can create three stent architectures, including rhomboidal, sequential zig-zag rings and sinusoidal spiral. Parameters are used to create a G-code sequence, where virtually any architecture can be designed and produced via code (

Figure 3.3). DFC decreases printing speed to ensure the bond between struts at joint points. DFC was beneficial for rhomboidal stents improving mechanical properties. These under extrusion zones are explained furthermore during the printing process of SMS and HMS.

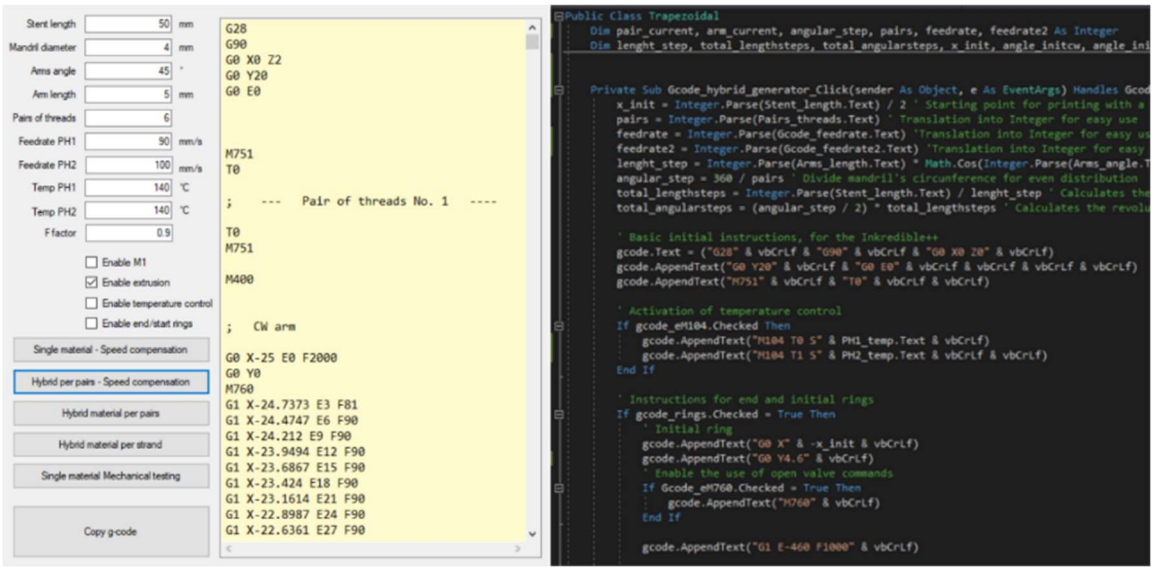

Figure 3.2. G-code generator. A G-code generator was created to produce parametric G-code instructions with a user-friendly interface.

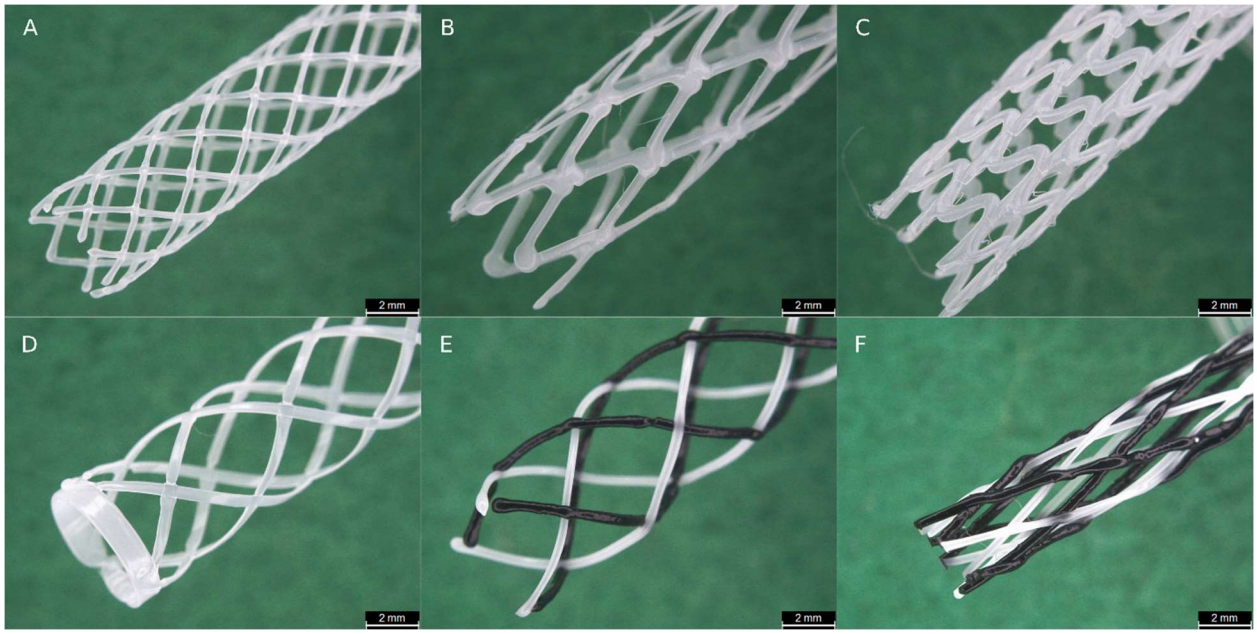

Figure 3.3. PCL stent architectures with different mandrel diameters fabricated using the Hystent printer based on the generated G-code. A, rhomboidal. B, zig-zag. C, sinusoidal. D, rhomboidal with end rings. E, PCL/GO HMS. F, PCL/GO HMS. Stent internal diameter: A-D 4mm, E 5mm, F 2.5 mm.

The software compensates stent dimensions to fabricate complete structures in the range of the specified parameters. Thus, a 15 mm stent will be generated as 3 consecutive rings of 5mm even when a 5.2 mm ring was requested. Auto-adjusted dimensions can be disabled in favor of dimension accuracy.

The basic movement to print a stent by using a rotary-axis involves a linear movement along the X-axis with a synchronized angular movement. The change from the common cartesian XYZ to an angular-XYZ can be confusing at first glance. Also, this approach involved more calculations and sequence repetitions. However, a systematic approach was sought to simplify G-code generation, stents were divided into basic sequences. This sequence repetition is the key element during stent design and coding. Once the essential structure is isolated, this can be

divided into subsections for easier calculations. The structure is repeated as needed to fabricate a complete stent. Certain stent designs involved a slightly different approach, but simplification into an essential structure remains as the first design step.

3.2.1. Rhomboidal stent

For rhomboidal stents, the basic sequence is a pair of lines that intersect to form the rhomboidal structure. The lines are a sequence of linear-steps synchronized with angular-steps at a defined printing speed (Figure 3.4). Linear steps were related to the strut length and the angle (φ) between struts (Equation 3.1). The angular-step, the rotation needed to print one linear-step, is the product of the number of pairs of lines (PofL) to print along the mandrel circumference (Equation 3.2).

$$\boldsymbol{Linear\ step = StrutL * \cos(\varphi)} \qquad \text{Equation 3.1.}$$

Linear steps to print a rhomboidal stent, the distance over the X-axis to produce a complete rhomboidal structure. StrutL, the longitude of the strut arm.

$$\boldsymbol{Angular\ step = \frac{360°}{PofL}} \qquad \text{Equation 3.2.}$$

Angular steps to print a rhomboidal stent, rotation needed for the rotary axis to produce a complete linear step. PofL, number of pairs of lines for the stent.

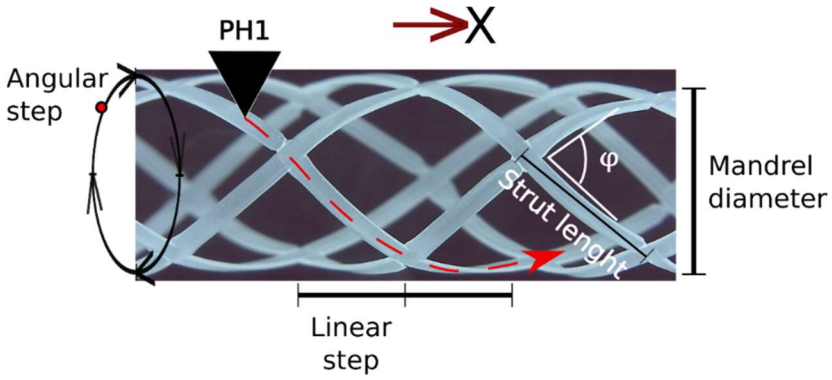

Figure 3.4. Rhomboidal stent essential unit. An angular step correlates to a linear step over the X-axis in the function of arms length and struts angle (φ).

The sequence is repeated to complete a stent with the desired length. Every pair of lines are symmetrical to each other, one clockwise and the other counterclockwise. Both lines share the same initial point with the next and previous pair of lines, e. g., for struts at 45°, the first strut starts at 0° and the complementary strut at 45°. The second pair starts at 45° and its complementary at 90°. This sequence is repeated to cover the mandrel circumference (Figure 3.5). Printing speed, specified as feedrate, was tuned to allow consistent material dispensing at the desire strut diameter.

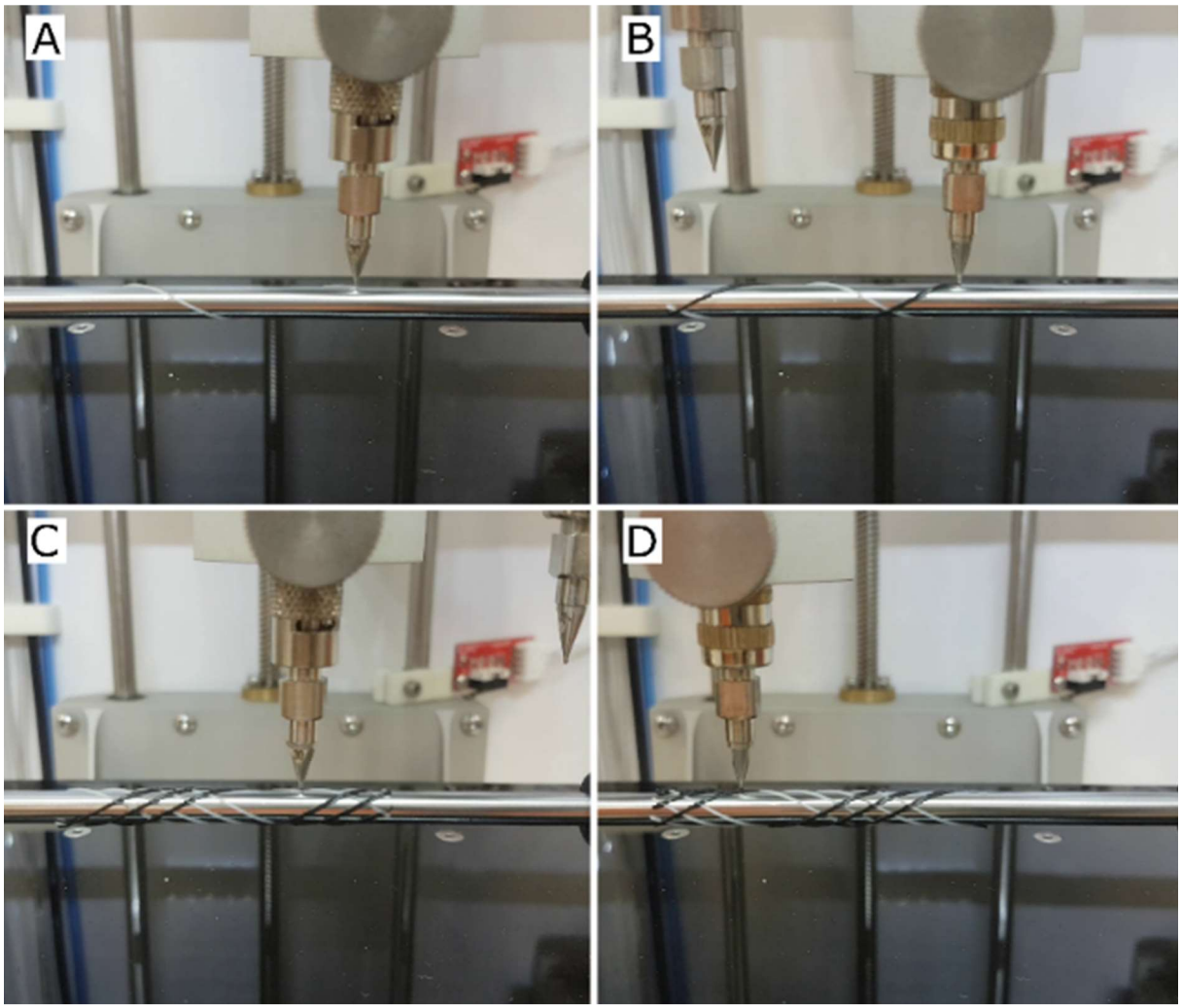

Figure 3.5. The hybrid-material printing process for rhomboidal stents. Printed lines were calculated as sequence single linear and angular steps to form a rhomboidal shape (A-B), these sequences were repeated to fabricate a complete stent (C-D). Mandrel 5 mm, Nozzle ID 400 µm.

3.2.2. Zig-zag stents

The essential unit of a zig-zag stent is the pair of v-shaped arms. The zig-zag sequence is a linear step forwards and a linear step backward. Every sequence required one angular step according to the strut angle. For this stent design, either arm length or arm angle must be fixed to obtain complete units along the rotary-axis circumference due to their geometrical correlation. Every sequence uses the last printed arm as the starting point (Figure 3.6). Once a ring was completed the next ring of zig-zag elements was printed after a fixed offset. This offset considers nozzle diameter, stent length and the number of intended rings to print. The latter was also adjusted to print complete zig-zag rings along the specified stent length. An organic over-extrusion zone occurs at the joint points on this design due to the change in direction under continuous flow. DFC could be implemented to reduce these over-extrusion joints.

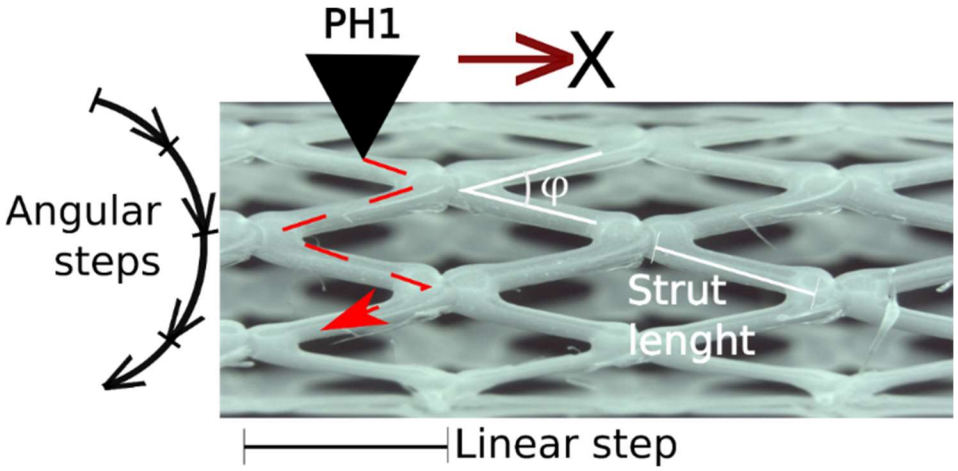

Figure 3.6. Zig-zag essential unit. To print a zig-zag unit to the specified strut length, one angular step is required dictated by the strut angle (φ).

3.2.3. Sinusoidal stents

For sinusoidal stents, the basic sequence is a sinusoidal wave along the mandrel transversal perimeter. These sinusoidal units are calculated based on wavelength and wave amplitude. Every sinusoidal structure is printed tilted to allow a full rotation plus a wave amplitude offset (Figure 3.7). The number of sinusoidal structures was adjusted to print complete sequences along the mandrel perimeter. A full rotation was divided into angular steps, one angular-step was calculated as the rotation needed to print a sinusoidal unit (Equation 3.3). The linear step was calculated as a sinusoidal function of wave amplitude (Equation 3.4). After a sinusoidal structure is printed a strut connector is printed bonding into the next one to improve structural support in an otherwise lose spring-like structure.

$$\boldsymbol{Angular\ step} = \frac{\boldsymbol{Desired\ Wave\ length}}{\boldsymbol{2\pi\ Rod\_radious}} \qquad \text{Equation 3.3}$$

Angular steps for sinusoidal stents were calculated based on the sinusoidal wavelength and the rod radius.

$$\boldsymbol{Linear\ step} = \boldsymbol{Sin}(\boldsymbol{\varphi})\left(\frac{\boldsymbol{Wave\ amplitude}}{\boldsymbol{2}}\right) \qquad \text{Equation 3.4}$$

Linear steps were the printhead travel distance to print half sinusoidal wavelength at the desired initial angle (φ).

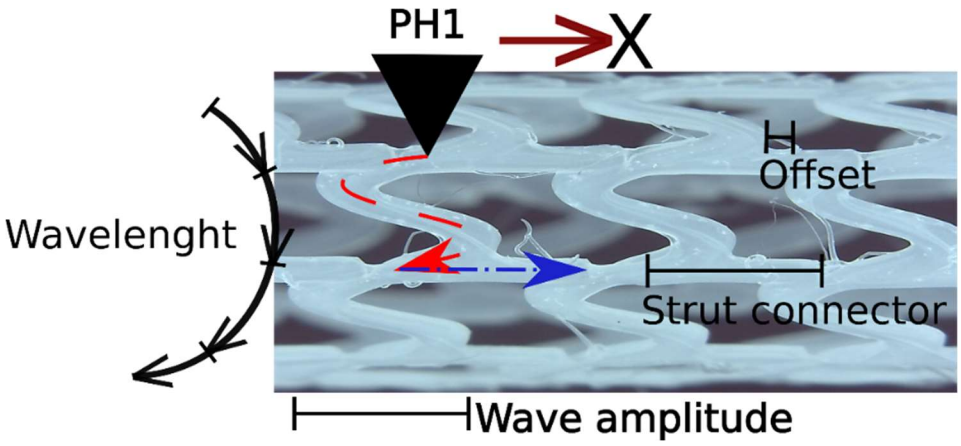

Figure 3.7. Sinusoidal essential unit. Based on wavelength and wave amplitude a sequence of sinusoidal structures was printed along mandrel transversal perimeter with an offset in the X-axis. A strut connector was added for structural support

3.3. Thermogravimetric analysis

The thermal stability of PCL and PCL composites was measured by using TGA. EFG-based nanofillers and composite were tested as received from another research group in this lab. Thermal curves were analyzed with a macro in the manufacturer software (Appendix C).

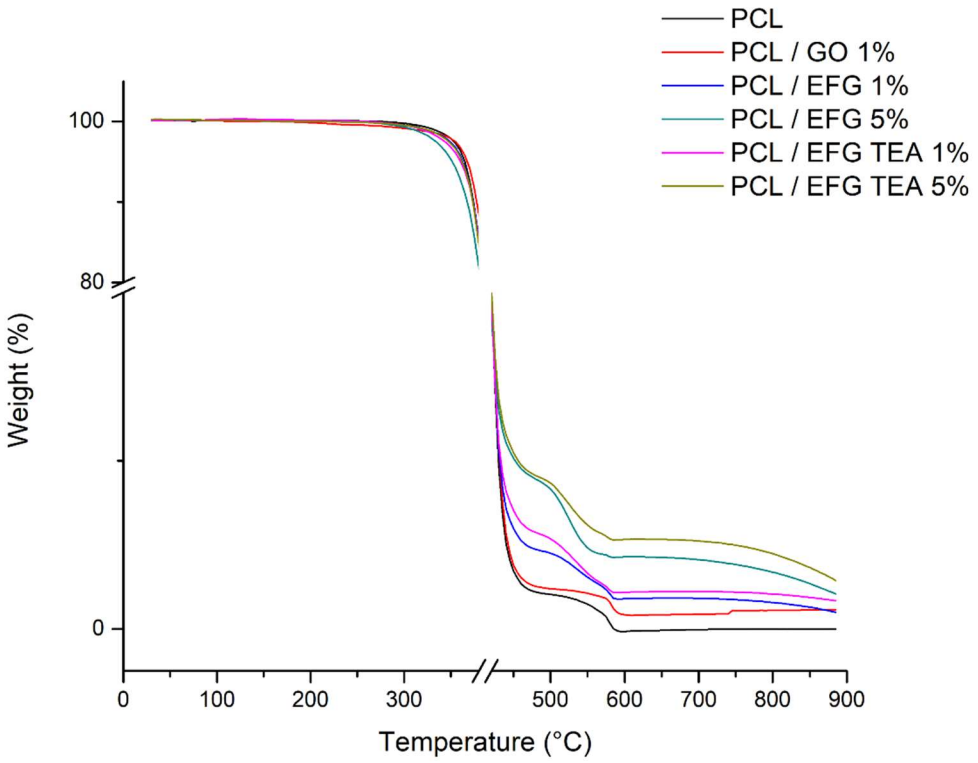

Figure 3.8. Thermogravimetric curves for PCL and graphene-based composites. All samples were heated up to 600 °C in a nitrogen-rich environment, afterward, air was introduced to allow oxidative reactions.

The addition of graphene-based nanofillers had a minor impact on thermal stability or decomposition temperature of PCL [51,57]. These results showed that PCL and PCL-composites remained stable up to 370 °C, which is well above the printing temperature (Figure 3.8), indicating that there is no risk of polymer decomposition during printing. The nanofiller content in composite with 5 wt% EFG content was lower than expected, although between error margin (Table 3.1). This can be linked to the manufacturing process where some material may be lost during coagulation and washing steps.

Table 3.1. Thermogravimetric properties of graphene-based composites. Relative nanofiller content was measured based on PCL residues at 700 °C.

	Temperature at 10% weight loss	Decomposition temperature	Relative nanofiller content

	°C	°C	wt %
PCL	374.20 ±0.92	377.17 ±0.97	0 ±0.28
PCL / GO 1%	377.75 ±1.36	381.95 ±1.74	0.84 ±0.83
PCL / EFG 1%	374.04 ±3.02	378.38 ±3.72	1.18 ±1.15
PCL / EFG 5%	376.45 ±1.95	376.45 ±2.38	3.21 ±0.44
PCL / EFG TEA 1%	373.68 ± 2.05	377.67 ±2.32	1.32 ±0.49
PCL / EFG TEA 5%	373.45 ±1.01	377.53 ±0.49	4.32 ±0.93

3.4. Differential scanning calorimetry

Differential scanning calorimetry was performed to evaluate the effects of graphene-based nanofillers in crystallinity, melting and crystallization temperature of PCL composites. Samples were encapsulated into aluminum pans with weights from 6.1 – 12.5 mg. Crystallinity was calculated with PCL enthalpy at 100% crystallization (139.3 J/g) (Equation 2.1) [30,58].

Table 3.2. Crystallinity percentage, crystallization and melting temperatures for PCL and PCL graphene-based composites.

Material	T_c °C	T_m °C	α %
PCL	26.01	55.82	0.44
PCL / GO	31.66	56.87	0.43
PCL / EFG 1%	33.63	56.38	0.43
PCL / EFG 5%	36.28	56.04	0.48
PCL / EFG TEA 1%	33.92	56.88	0.43
PCL / EFG TEA 5%	35.98	56.58	0.44

Tc, crystallization temperature. Tm, melting temperature. α, crystallinity

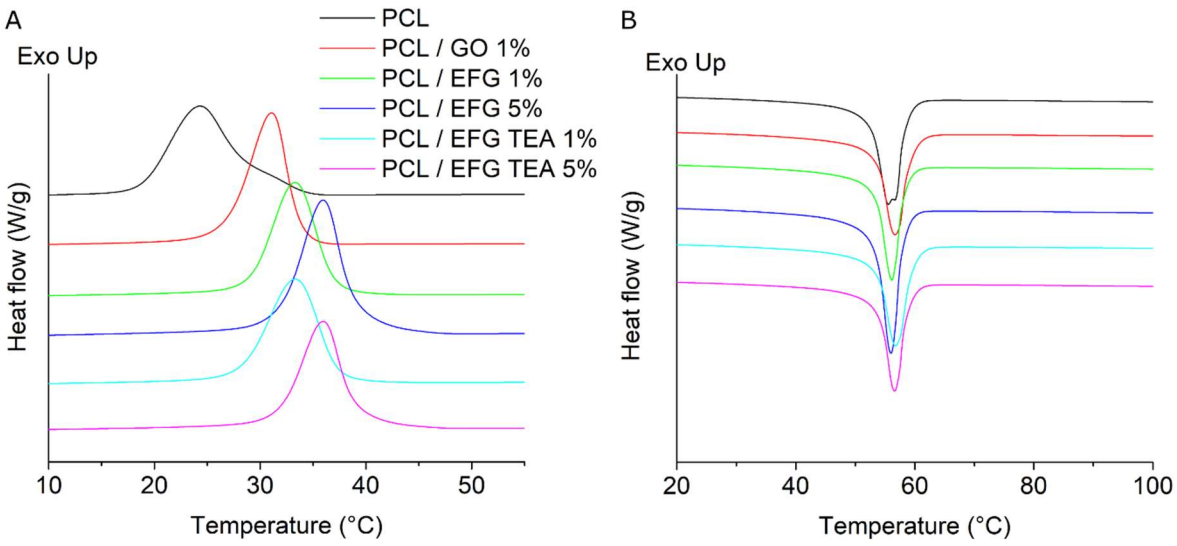

Figure 3.9. Offset thermograms at crystallization and melting temperature. A, Crystallization temperature. B, Melting point. Exothermically reactions registered upwards.

The addition of graphene-based nanofiller in PCL composites increased the crystallization temperature with minimal effect on melting temperature or percentage of crystallinity. Crystallization temperature changes can be explained by the increase of nucleation sites with graphene-based nanofillers [51,59]. In regards to crystallinity, the incorporation of these graphene-based nanofillers has a neglible impact on the PCL structure, hence composite degradability may be preserved [30]. Based on these thermograms, PCL and PCL-composites melted at similar temperatures, albeit the differences in crystallinity might modify rheology properties and printing protocols.

3.5. Rheological properties

The impact of graphene-based nanofillers on the viscosity of the PCL composites was measured versus shear rate (0.001 to 100 s^{-1}) at 120°C (Figure 3.10) as well as the temperature at a constant shear rate (1 s^{-1}) (Appendix D). All graphene-based composites demonstrated a shear-thinning effect. The shear-thinning effect is due to the unentanglement and flow alignment of the polymer chains under higher shear rates [60]. However, GO 1%, EFG 5% and EFG TEA 5% showed a higher viscosity vs shear rate compared to the other samples. This increase in viscosity may be explained by the higher nanofiller content in the EFG-based composites and stronger interactions between

nanosheets with PCL chains due to higher functional groups in GO [61]. These interactions were evident by the higher degradation temperature of PCL / GO composite and lower feedrate required for adequate printing. In contrast with EFG lower disorder as demonstrated by the Raman spectroscopy (Figure 3.22) and higher feedrate needed for printing [30,62,63].

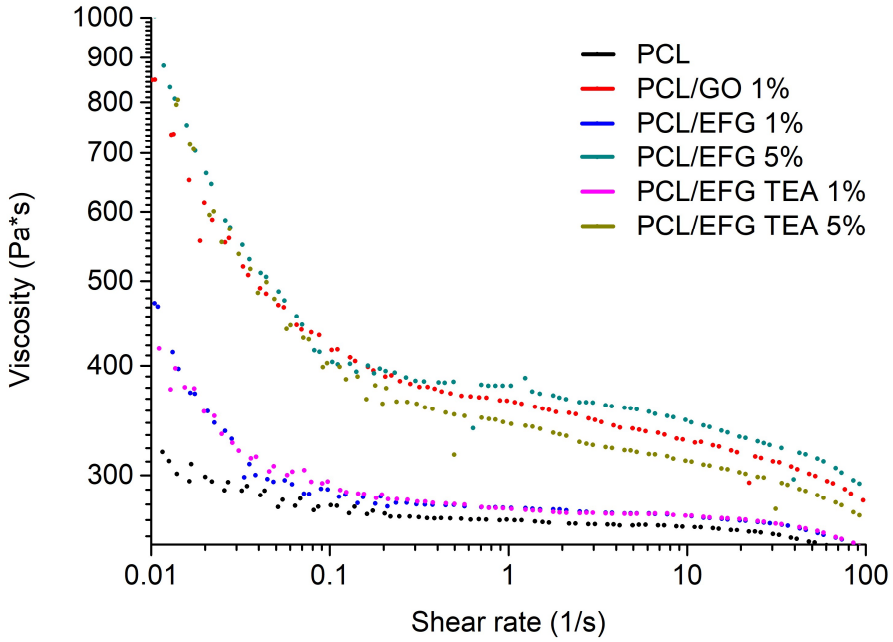

Figure 3.10. Viscosity curves of PCL and PCL / graphene-based composites vs shear rate. The measurement was recorded at printing temperature, 120 °C.

Rheology data provided the rationale behind the printing protocols for each material (Table 3.3). From these printing parameters, feedrate is the only parameter that can be modified swiftly via G-code during printing.

3.6. 3D printed single-material stents

Bioabsorbable polymers have lower mechanical properties compared to their metallic counterparts [9,15]. Also, the strut diameter plays a major role in the implantation procedure, vascular healing, and remodeling [42].

Currently, BRS struts are less than 150 µm in diameter [9]. This section was aimed to develop a BRS with clinically relevant strut dimensions and mechanical properties.

Table 3.3. Printing feed rates for graphene-based composites to print rhomboidal stents.

Material	Feedrate mm/min
PCL	40
PCL / GO 1%	30
PCL / EFG 1%	50
PCL / EFG 5%	40
PCL / EFG TEA 1%	60
PCL / EFG TEA 5%	50

Single-material stents were fabricated using the Hystent printer with pressurized cartridges with nitrogen at 300 kPa. The temperature was set at 120°C, above melting temperature, to offset heat loss due to high heating block volume and scarce thermal isolation. Strut dimensions proved to be feedrate sensitive. Hence, feedrate was set for each graphene-based composite (Table 3.3) to obtain round fibers with a 275 µm average diameter.

The rhomboidal stent design was selected as a test subject, it was designed with six pairs of struts with a strut length of 2.5 mm, 45° angle and 4 mm ID. This rhomboidal design allowed different configurations with symmetrical distributions for single- and hybrid-material. To achieve the average diameter struts of 275 mm struts, feedrate was changed according to the printing material (Table 3.3). Strut diameter was highly sensitive to feedrate with the advantage of being handled easily by the G-code generator. Other measures were tested to control the strut diameter, such as temperature and cartridge pressure. As previously mentioned, higher temperatures decrease PCL viscosity with the disadvantage of allowing the graphene nanoplatelets to agglomerate resulting in nozzle blockage. Also, a significant increase in cartridge pressure during printing with low material volume could yield the surface tension allowing the nitrogen to flow through the melted polymer instead of pushing it through the nozzle.

As mentioned previously, joint points were a sensitive region for the rhomboidal stent. After the nozzle passes over a join-point, an under-extrusion region was observed. To tackle this issue, dynamic feedrate compensation (DFC) was incorporated into the G-code generator software. DFC decreases the printing speed before and after the joint point, thus creating an over-extrusion zone that preserves the cohesive force and creating stronger joints. A

similar strategy can be implemented on other stent architectures were sudden changes in direction produce over-extrusion regions. DFC can be used to increase the printing speed in those regions.

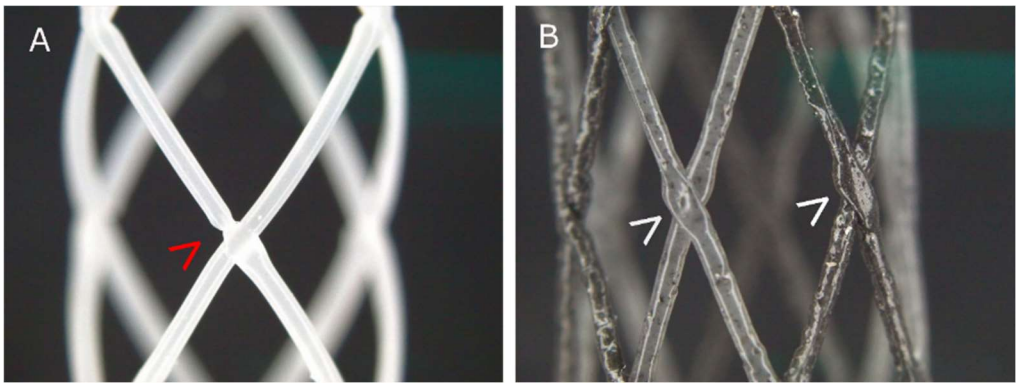

Figure 3.11. A fixed printing speed produces weak joints (red arrowhead). DFC creates over-extrusion zones (white arrowhead) by decreasing printing speed before and after a join. A, PCL-stent printed using fixed feedrate. B, hybrid-material stent printed using DFC

3.7. Mechanical testing of single-material stents

SMS were printed using the Hystent printer with a rhomboidal design with on average 275 µm strut diameter. Feedrate compensation was set at 0.5. Due to printer resolution and the mechanical tolerances of a RepRap system, printing reliably below this dimension proved to be a challenging process. Strut dimensions were aimed to mimic, as close as possible, the dimensions of commercially available stents. The strut thickness of commercially-available stents ranges between 50 µm and 140 µm. Lower strut thickness is associated with a lower incidence of LSR [39], hence the importance of achieving a low profile strut and stent. SMS were printed with the material described in Table 3.3. There was no significant difference in strut diameters among all SMS. After printing, stents were attached to a custom-made 3D-printed clamp adaptor using epoxy glue (Appendix A). Mechanical properties of the stent were recorded by axial compression (Figure 3.12) tensile testing (Figure 3.13) and cyclic radial (Figure 3.14).

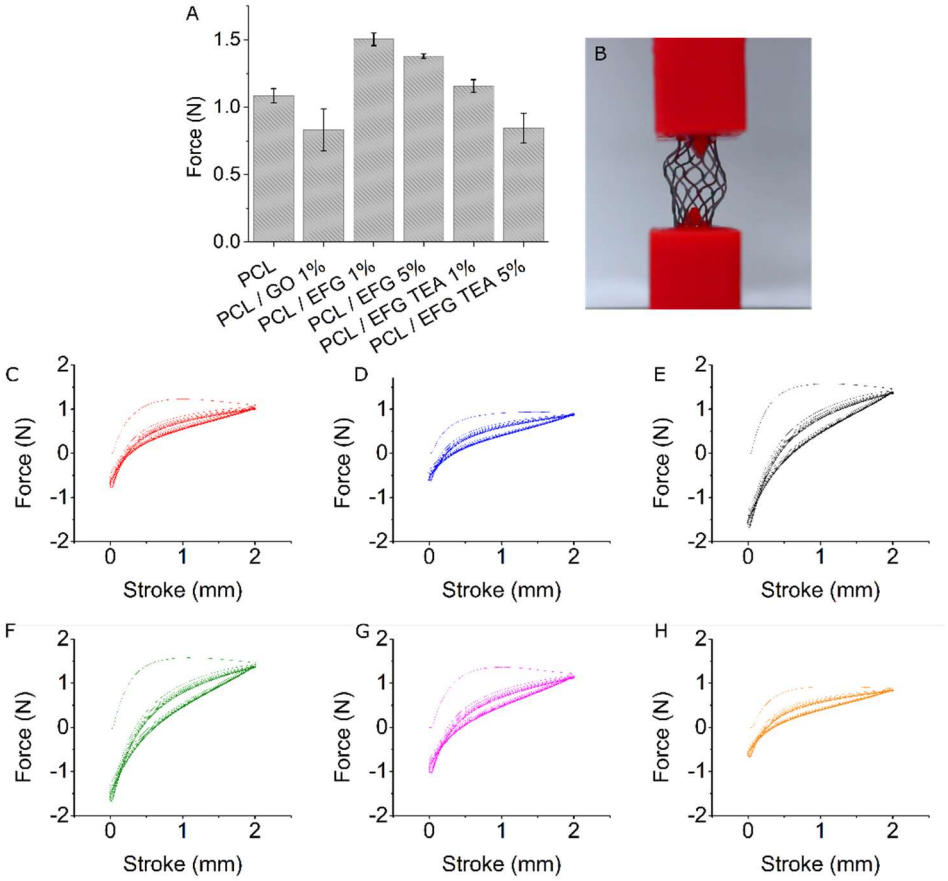

Figure 3.12. Force and stroke curves for axial cyclic compression of PCL-based single-material stents. A, average load per material (n=4); error bars represent the standard deviation among samples. B, axial compression 2 mm stroke. C, blank PCL. D, PCL/GO 1%. E, PCL/EFG 1%. F, PCL/EFG 5%. G, PCL/EFG TEA 1%. H, PCL/EFG TEA 5%. Samples were tested 10 compressive cycles 2mm stroke at room temperature.

Axial and radial cyclic compression of single-material stents were used to measure the mechanical properties of the 3D printed stents. Under axial compression, all stents showed an initial large hysteresis that decreased by increasing the number of compression cycles (Figure 3.12. C-H). Average compression forces required to compress SMS stents by 2 mm for 10 cycles is compared in Figure 3.12, A. PCL/EFG 1% (1.50 N SD 0.05, $p<0.05$) and PCL/EFG 5% (0.71 N SD 0.9, $p<0.05$) exhibit the highest axial and radial compression strength, respectively. All samples

showed similar viscoelastic curves on both axial and radial compression tests with relatively similar force softening in all samples after 10 cycles. Compared to axial compression, radial compression showed small hysteresis indicating minimal initial deformation. Samples compressed more than 2 mm showed a greater deformation without recovery. Tensile tests were performed with stents attached to customized clamp adaptor. Force and stroke at break were recorded (Figure 3.13, C). Among all composites, PCL / EFG 1% showed the highest tensile strength (12.18 N SD 0.12, $p<0.05$) with a stroke at break higher than any other of the tested composites (1.39633 mm SD 0.40, $p<0.05$).

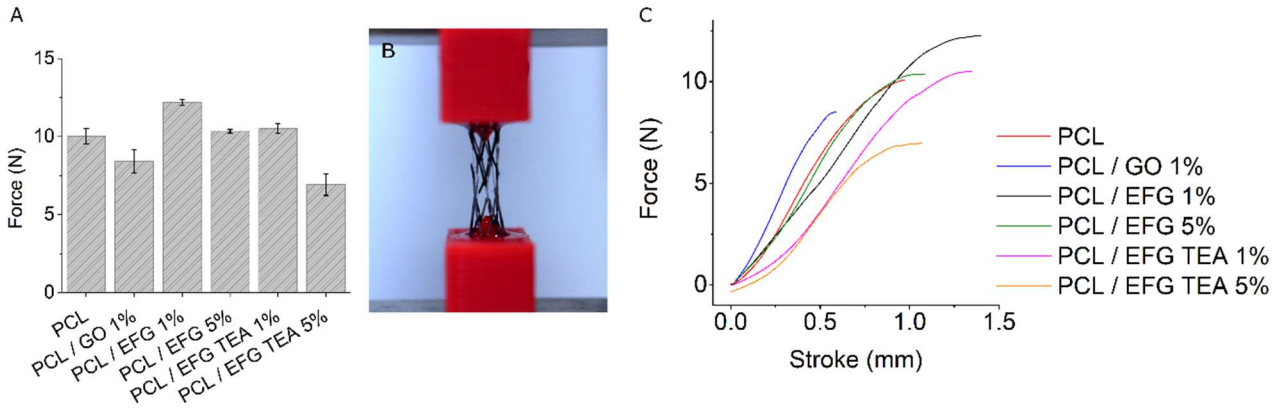

Figure 3.13. Tensile force at break of PCL-based stents. A, average load per material (n=4); error bars represent the standard deviation among samples. B, tensile test until breakage 2.5 mm maximum stroke. C, Tensile force single-material printed stents.

To fabricate HMS, PCL / EFG 1% was chosen based on higher strength and printability performance. Stent fabrication with this composite was a reliable procedure. However, it was acknowledged that EFG dispersion was not ideal and the clustering effect was increased after printing, albeit this composite showed promising results. Improving EFG dispersion in PCL requires further optimization beyond the scope of this research. HMS fabrication and mechanical testing will be discussed in the next section.

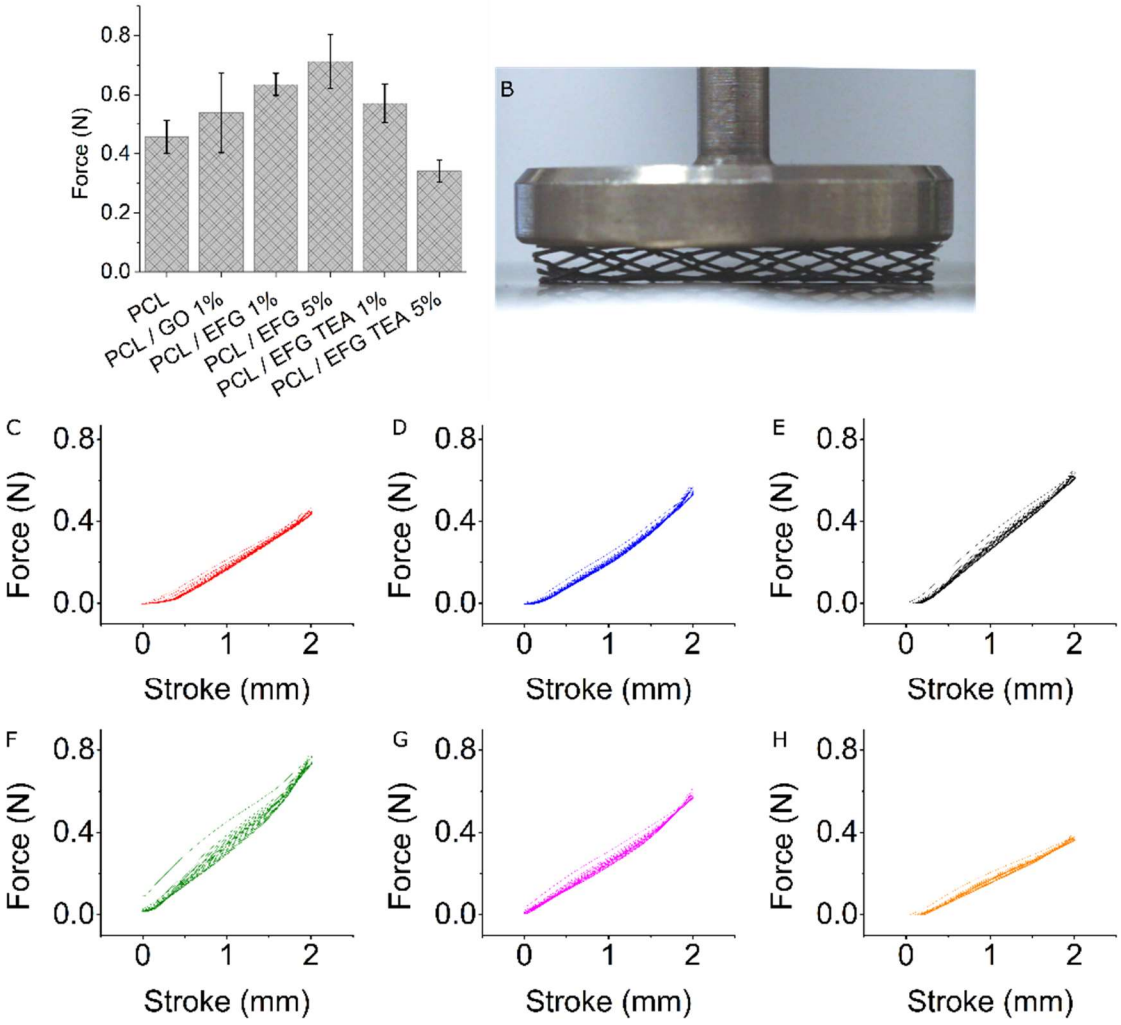

Figure 3.14. Force and stroke curves for radial compression of PCL-based stents. PCL/EFG 5% stents exhibit a higher radial compression force at a 2 mm stroke for 10 cycles. A, average load per material (n=4); error bars represent the standard deviation among samples. B, axial compression 2 mm stroke. C, blank PCL. D, PCL/GO 1%. E, PCL/EFG 1%. F, PCL/EFG 5%. G, PCL/EFG TEA 1%. H, PCL/EFG TEA 5%

Mechanical testing of single-material printed stents showed the benefits of the addition of graphene-based nanofiller such as GO and EFG. Overall, PCL / EFG 1% outperformed the other materials, especially in tensile strength and axial compression. EFG 5% showed higher compressive strength, a key feature of a clinically relevant stent.

EFG/TEA composites showed lower mechanical properties than blank PCL. EFG/TEA composites showed lower mechanical performance compared to the other EFG-based composites. Comparing with the other EFG-based composites, EFG/TEA composites required higher feed rate during the 3D printing. This may suggest high aggregation of EFG into polymer matrix that resulted in a poor polymer-polymer and polymer-filler interactions. Further work is required to investigate the interaction between this filler and PCL and its effect on the properties of PCL.

.

3.8. Hybrid-material stent printing

To fabricate HMS, dual-PH capabilities of the Hystent printer were used. Dual-PH printers present some challenges such as rotary-axis functionality and axis alignment. This is an inherent issue of any dual-PH printers. For X and Y alignment, two strategies were useful, firmware-based and G-code compensation. In firmware-based compensation, the firmware was modified to account for the second PH offset with the downside that every nozzle change would require readjustment and the readjusted firmware must be flashed. This process can be time-consuming but reliable. In G-code compensation, the G-code was modified to account for the position of the second PH. This strategy could be swiftly implemented but increases the likelihood of error and print failure. The firmware-based compensation was selected, once the Hystent printer was aligned and calibrated with the selected nozzle there was no need for further adjustments.

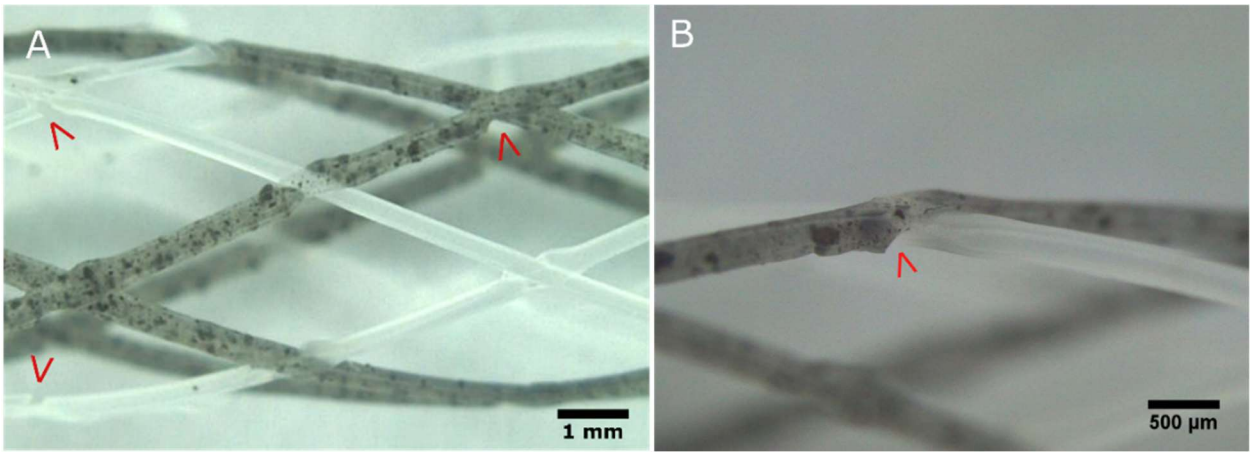

Figure 3.15. Hybrid-material stent under-extrusion zones immediately after the joint points (red arrowheads). HMS blank PCL and PCL/EFG 1%.

HMS was printed PCL and PCL / EFG 1% composite in a complementary arrangement. A rhomboidal stent was fabricated with six pairs of struts using half of the struts printed using PCL and the rest with PCL / EFG 1% composite. Printing protocols were followed according to Table 3.3 no printing failures were encountered during HSM printing after proper nozzle alignment was performed. During the rhomboidal stent fabrication, under-extrusion zones were detected (Figure 3.15). These regions had a major impact on HMS mechanical properties, trying to solve this issue DFC was implemented. DFC decreases printing speed to allow more material to be dispensed at the junction point, reducing this under extrusion zones. DFC implementation increased HMS stiffness drastically, HMS structural performance was below that of SMS. There was no linear correlation between stiffness and DFC higher than 50%. Even with a DFC setting at 95%, under-extrusion zones were still present. Further research must be performed to shed light on the interactions of the different materials during HMS printing.

3.9. Degradation profile of hybrid-material stents

To test the degradation profile of HMS a preliminary enzymatic degradation study was conducted. HMS was exposed to a Lipase solution from *Pseudomonas* sp. for 24, 48 and 72 h (Figure 3.16).

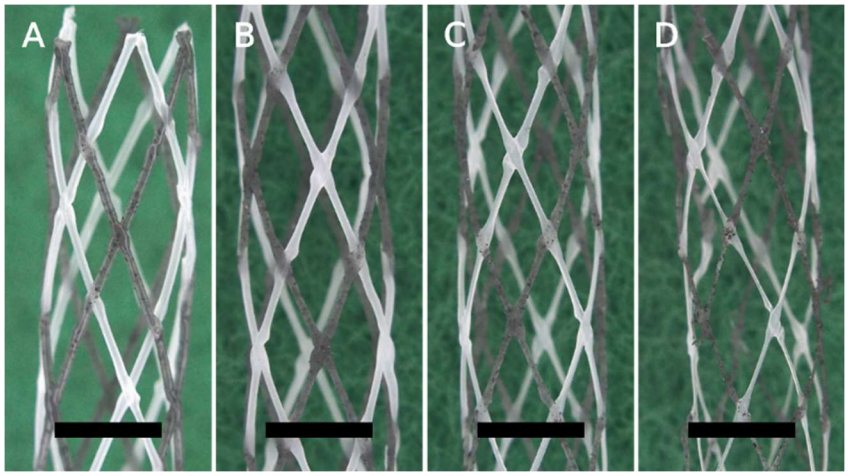

Figure 3.16. Enzymatically degraded hybrid-material stents. HMS was enzymatically degraded, Lipase from Pseudomonas sp. (type XIII). There are minimal differences between PCL and EFG 1% composite struts. A, before enzymatic degradation. B, after 24 h. C, after 48 h, D, after 72 h. 2 mm scale bar

Table 3.4. Weight of degraded HMS.

Weight of degraded HMS			
Time	Prior	Post	Weight loss
h	mg	mg	%
24	26.30 ±1.36	20.48 ±1.53	22.14
48	26.14 ±1.27	15.61 ±1.22	40.29
72	22.96 ±2.62	8.09 ±2.10	64.76

As shown in Table 3.4, samples lost on average 22.1%, 40.3, 64.8% fo their weight after 24, 48 and 72h of enzymatic degradation (Table 3.4). These results are difficult to match up with *in-vivo* conditions due to the different factors involved beyond hydrolytic degradation [64]. This degradation pattern was lower than expected for pure PCL with a reported enzymatic weight loss of 50 - 60% in the first 24 h [55]. More interestingly, after 24 h they reported a weight loss plateau, this trend was not present for HMS. This indicates that EFG-based composites modified the enzymatic degradation profile of PCL. A prolonged hydrolytic degradation study, including the rest of the graphene-based composites against blank-PCL, in near intravascular *in-vivo* conditions, is needed towards clinically relevant HMS.

3.10. SEM imaging

Surface imaging was obtained to investigate the influence of degradation on the surface topography of stents (Figure 3.17). Samples were platinum coated and imaged in near-vacuum. No current variations were reported during imaging due to the presence of graphene-based molecules.

Enzymatic degradation was uniform along the observed areas, with a significant increase in composite porosity due to enzymatic degradation. This increase in porosity can increase the amount of drug eluted by the stent [65]. Although the surface appears minimally affected after 48 h of enzyme exposure (Figure 3.17, C), the mass loss at 48 h was more than 40% (Table 3.4) modifying significantly the mechanical properties of HMS. SEM images exhibit the bulk degradation pattern expected for enzymatic degradation [64,66]. Cross-sectional SEM images of non-degraded struts of the PCL-based composites used in this research are provided in Appendix F.

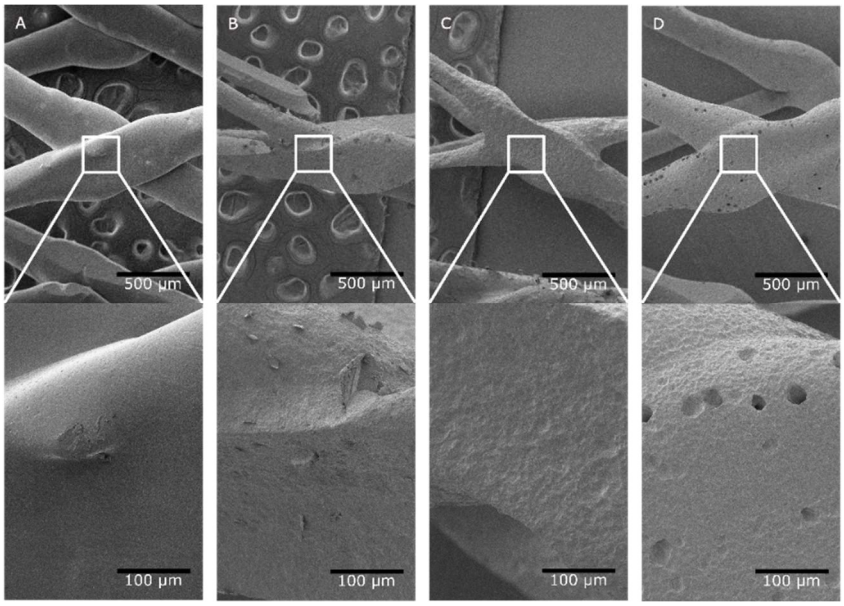

Figure 3.17. SEM images of HMS enzymatically degraded hybrid stents. According to the enzymatic exposure time: A, no exposure; B, after 24 h; C, after 48 h; D, after 72 h.

3.11. Mechanical testing of degraded hybrid-material stents

Mechanical properties of degraded HMS were tested through cyclic axial and radial compression, as well as tensile testing. Before degradation, HMS showed a lower strength in comparison with PCL and PCL / EFG 1% SMS across all mechanical tests (Figure 3.18), which can be attributed to under extrusion zones at HMS joints points.

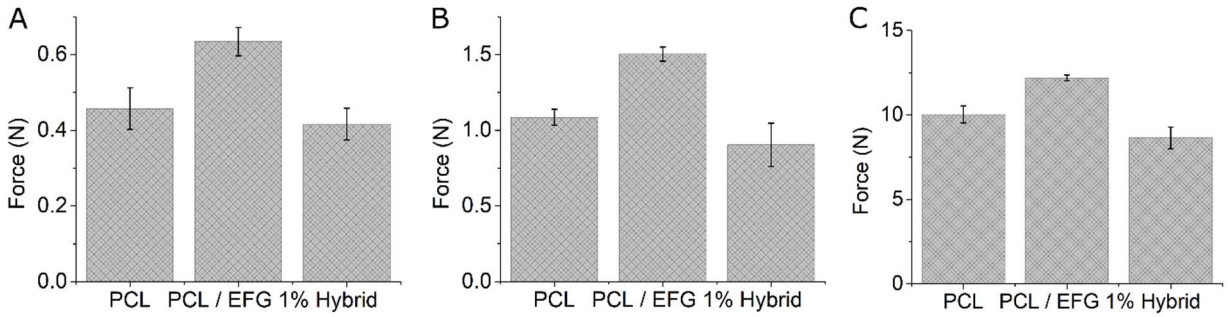

Figure 3.18. Average mechanical test results for PCL, PCL / EFG 1% and HMS. A, radial compression. B, axial compression. C, tensile test. Radial and axial compression 2 mm stroke. Tensile test at break maximum 2.5 mm stroke. Error bars represent the standard deviation among samples.

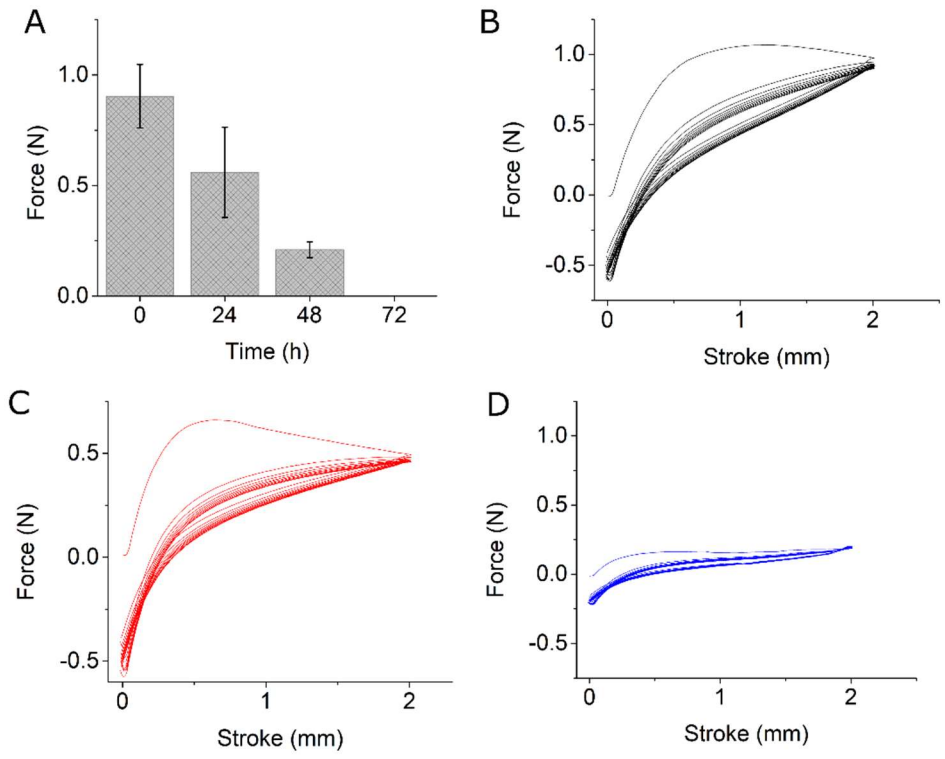

Figure 3.19. Axial compression of degraded HMS. A, average axial compression; error bars represent the standard deviation among samples. Samples after enzyme exposure at B, 0 h. C, 24 h. D, 48 h of degradation. 10 compression cycles, 2 mm stroke.

At first, these faulty joints were caused by a misalignment in the printhead, thus the over-extrusion zones were misplaced, stents were discarded. After PH alignment, HMS strength increased on average by 32%, albeit inferior to their SMS counterparts in every mechanical test. Under-extrusion zones were not completely corrected even after decreasing printing feedrate using DFC by 90% (Figure 3.15, red arrowhead). These results exposed the joint points, and their integrity, as crucial for printed stents, especially for rhomboidal stents. Under-extrusion zones must be addressed as the next step for HMS fabrication. By increasing the degradation time, a decrease was observed in the average axial force required to compress the degraded HMS samples by 2 mm (Figure 3.19). However, the elastic recovery behavior of the samples was minimally affected. A similar pattern was observed for

radial compression where HMS radial strength decreased along with the increased degradation exposure while maintaining a similar elastic recovery behavior (Figure 3.20). After 48 h of enzymatic degradation, HMS axial strength decreased by 76.8%, tensile strength by 41.6% and radial strength by 35.8%. HMS degraded for more than 48 h were too damaged to reliably measure their mechanical properties and were not included. It is worth noting that in this preliminary study stent degradation was irregular mainly in the bottom part. These could be an indirect marker of enzyme sink that requires further research.

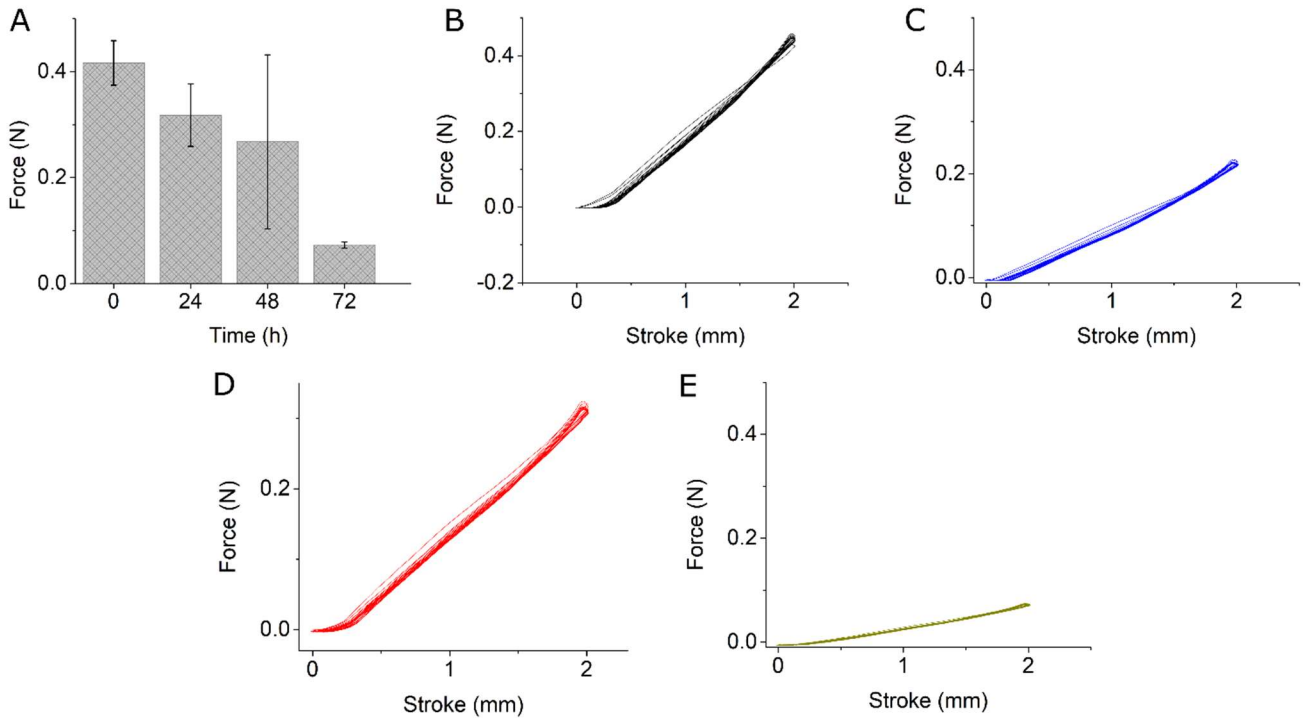

Figure 3.20. Radial compression of degraded HMS. A, average radial compression; error bars represent the standard deviation among samples. Samples after enzyme exposure at B, 0h. C, 24h. D, 48h. E, 72h of degradation. 10 compression cycles, 2 mm stroke.

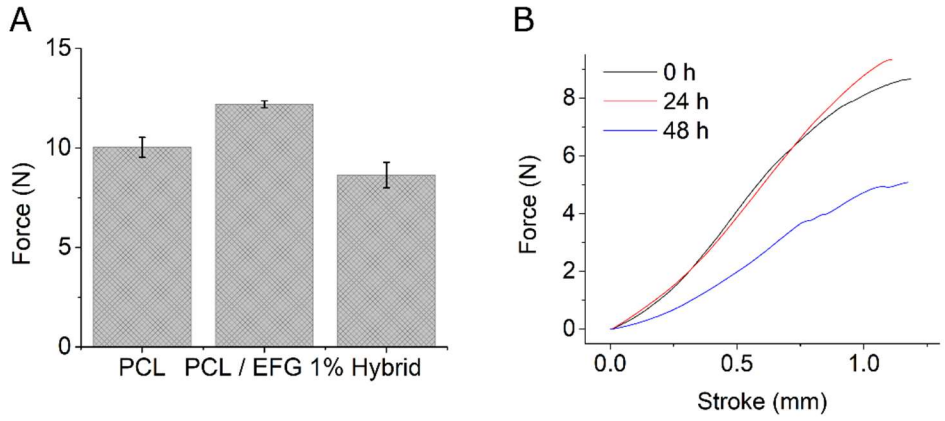

Figure 3.21. Tensile load tests for degraded HMS. A, average tensile load; error bars represent the standard deviation among samples. B, 0 h. C, 24 h. D, 48 h. Tension at breakage maximum stroke 2.5 mm.

3.12. Raman spectroscopy for PCL-based composites

Raman spectroscopy offers a non-destructive method to characterize crystalline and amorphous graphitic materials [62]. In this work, Raman spectroscopy was used for the characterization of EFG and Pcx-loaded composites (Figure 3.22). Pcx 1% (wt/wt) was loaded into PCL and PCL / EFG 1% composite to assess the drug-eluting capabilities of EFG-based composites. Pcx has a peak range at 1050-1093 and 1608-1681 cm^{-1} representing C-O stretching and C-C stretching, respectively [67,68]. EFG has two significant peaks at 1337 and 1602 cm^{-1} corresponding to D and G bands [63,69]. PCL presents peaks at, 1060 and 1106, 1281–1305 range, and at 1726cm^{-1}. The first two peaks represent skeletal vibrations; the second, CH2 groups; and C=O bonds in the last place [51]. In Figure 3.22 the presence of Pcx 5% in both composites, PCL and PCL / EFG 1% composite is shown. However, the EFG G band in the PCL/EFG1%/Pcx 5% composite can be seen as a discrete double hump in combination with the PCL C-O bonds around 1600 cm^{-1}. EFG D band is hardly visible due to the overlapping signal of CH2 groups in PCL.

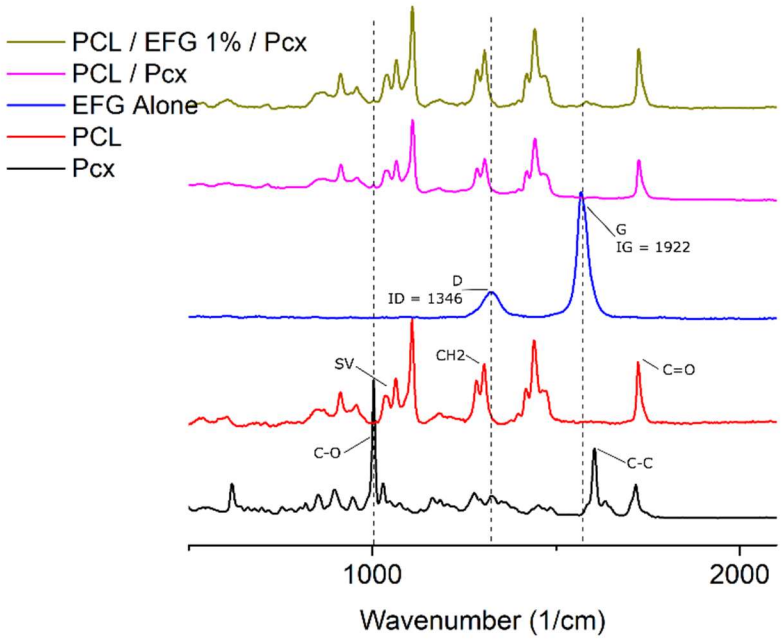

Figure 3.22. Raman spectroscopy of paclitaxel-loaded PCL and PCL/EFG 1% composite.

Graphene-based materials under Raman spectroscopy have D and G bands [67,68]. These bands represent the disorder and crystalline structure of graphene. D band is the result of structural disorders. The G band shows the crystalline structure of sp^2 carbon networks. The intensity ratio of D and G band (I_D/I_G) has been used for the characterization of defects in graphene-based materials [70]. In EFG, a low I_D/I_G of 0.70 was recorded, thus the measured area might be considered as a low defect zone. In contrast with previously reported Raman spectroscopy that showed highly disordered GO due to a high I_D/I_G caused by the presence of sp^3 carbon atoms and multiple hydroxyl groups [71]. Raman spectroscopy results indicated incorporation of Pcx and EFG into the polymer host. However, more investigations are required to evaluate possible structural changes that may result from their interactions.

3.13. Hybrid-material stent drug-eluting estimation via HPLC

HPLC was used to test the impact of EFG 1% on the drug-eluting capabilities of PCL. HMS was printed using a rhomboidal design with 6 pairs of symmetrical struts, 3 pairs of struts were printed using PCL and the other 3 with PCL / EFG 1%. Two groups were created, PCL and EFG groups according to the material loaded with Pcx. After

fabrication, both groups were submerged in PBS/Tween 20 solution and incubated in a water bath at 37 °C. The first release sample collection was at 24 h, and then every 48 h over the course of release study (9 days).

In-vitro Pcx cumulative release measured by HPLC showed a sustained drug elution for up to nine days (Figure 3.23). Every stent was loaded with 1% Pcx in half of the struts, with an average total stent weight was 12 g, 60 µg of Pcx was loaded in every stent. After 216 h, 1.35 (±0.13738) and 0.94 (±0.02744) µg were cumulatively eluted from the PCL and EFG group, respectively. Both materials showed an initial spike due to Pcx on the stent surface and a final peak after 9 days. Eluting patterns were mildly different. PCL group showed a continuous release while EFG decreased to peak at the end of the experiment. Cumulative Pcx release was slower in the EFG group there were no statistically significant differences between groups at the same time point. These results demonstrated that the addition of 1% EFG decelerated the drug-eluting rate of PCL, remains to be seen a correlation between higher nanofiller content and reduced drug releasing rate.

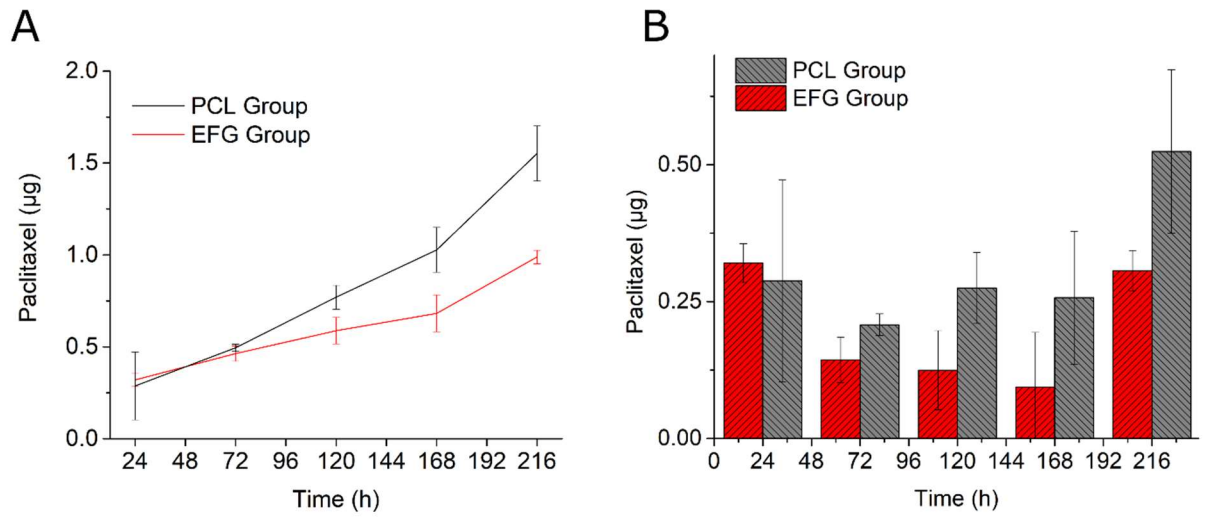

Figure 3.23. In-vitro release of Pcx-loaded HMS measured via HPLC. A, cumulative paclitaxel release; error bars represent the standard deviation among samples. B, average paclitaxel eluted at every time point; error bars represent the standard deviation among samples. PCL, paclitaxel-loaded blank PCL. EFG, paclitaxel-loaded PCL / EFG 1% composite.

4. Discussion

There is a need for a reliable printing process to achieve micrometric structures in the hundred-microns range capable of handling drug-loaded composites and hybrid-material structures. Previous work has shown the feasibility of polymer-based and graphene-based composite for BRS fabrication [19,20]. These BRS were limited by the printer capabilities or cumbersome post-processing to obtain a functional product. The Hystent printer using graphene-based PCL-composites made the fabrication of HMS with optimized mechanical properties a streamlined procedure. To the best of this author's knowledge, this is the first report of a customized HMS printer and 3D-printed HMS fabricated from graphene-based composites.

For BRS fabrication two stent printers having published using both similar setups, conventional FDM printers customized into stent printers. The first used a flat building plate and second a rotary axis as building surface [19,20]. The use of a flat building plate has the inconvenience of a post-printed crimping procedure with an increased risk of structural damage [19]. These printers were single nozzle systems that produced stents with strut width above 500 µm [20,72]. Furthermore, those were not configured to work in sterile conditions, a requirement for biomedical applications. The setup presented in this work is capable of printing stents reliably with a strut thickness of 275 µm configured in single- and hybrid-material architectures without further post processing steps. Using a bioprinter as a starting point enables us to work in sterile conditions to develop not only stents but cylindrical scaffolds for a myriad of applications. The Hystent printer is able to fabricate cylindrical structures using graphene-based composites for tissue-engineering, such as neural regeneration [73], esophageal prosthesis [40], vascular structures [74] and urethral reconstruction [75].

Graphene has been shown to improve the cytocompatibility of some materials and when used in low doses does not induce any notable short-term toxic effects in mice [35,38]. Drug-eluting capabilities and mechanical properties can be enhanced by the addition of graphene-based molecules. Also, antibacterial and antitumoral properties have been reported [19,34–37]. These characteristics make graphene-based nanofillers promising candidates for stent fabrication.

Graphene-based stents were mechanically superior to blank PCL stents with the downside of slower printing speed (Table 3.3). Although EFG-based composites require further optimization, the addition of EFG as a nanofiller

increased the overall stent strength while allowing a reliable printing process. At the same time, maintaining the drug-eluting capabilities of PCL.

Strut dimensions were aimed to resemble the average DES or BMS characteristics. An average of 275 µm strut diameter was achieved with a reliable printing process. Fabrication of struts with a thickness below 250 µm proved to be a challenging endeavor. Strut dimensions have a major impact on the performance of any stent [42]. The highest nozzle clogging rate was observed during 3D printing of stents from PCL GO 1% composites. Partial clogging could have caused inconsistencies during the printing process, thus higher sample to sample variability during mechanical testing. Stents fabricated using EFG-based composites showed a proportional change in printing speeds along with nanofiller content. Higher nanofiller content required slower feedrates, consistent with rheological results. Sample to sample variability for EFG-based composites could be explained by inconsistent nanofiller dispersion, which was more evident in samples with higher nanofiller content. Furthermore, PCL polymer chain degradation in the EFG-TEA group could be the cause of underperformance in the mechanical tests and higher variability compared to the rest of the material used in this project. During this research, particle size and nanofiller dispersion were not measured. Future work can tackle this by using strut diameter measurements in at least three sites in the length of the stents and improve composite manufacturing methods.

The use of composite materials increased SMS strength without increasing strut dimensions. On the other hand, the addition of EFG increased the tensile and compressive strength of PCL. The addition of 1% EFG increased axial strength by 27% and tensile strength by 23%, while 5% EFG increased radial strength by 36%. A similar strength increase with the addition of graphene-based nanofillers was found in the literature [76,77]. This may be explained by a strong interfacial interaction between the PCL matrix and the graphene-based nanofillers [71]. This trend from EFG 1% composite was not observed with EFG TEA composites, this might be an indication of an improper dispersion followed by nanofiller agglomeration during printing [71] or damage of the PCL fibers with the use of TEA. An optimized dispersion of EFG and EFG TEA could increase composite stiffness since dispersibility has a major role in graphene-based composites [71,77].

HMS underperformed SMS, where joint points played a crucial role. Joint points were under-extrusion regions and were the result of the interaction between three forces that occurred in the printing process. Pressure force

inside the cartridge pushes the polymer throughout the nozzle. Once the material is deposited onto the mandrel, an adhesive force keeps the polymer attached to the surface and, at the same time, a cohesive force pulls polymer out of the nozzle [78]. These forces were modified at the joint points, the cohesive force was nullified, thus creating an under-extrusion region (Figure 3.11). To tackle this issue DFC was implemented. DFC reduced printing speed before and after a joint point over extruding material at this critical site. After implementing DFC, HMS radial strength increased by 32%, but still underperformed SMS. The presence of joint-points added a level of uncertainbility . Besides joint-point optimization, it remains to be seen what different interactions between composites during printing can explain the underperformance of HMS mechanical properties.

Radial strength of SMS and HMS was inferior to the force needed to open a coronary artery, healthy or atherosclerotic, thus raising the need for sturdier composites to achieve similar mechanical properties of the commercially available stents [9,43,79]. HMS mechanical properties were difficult to correlate with commercially available BRS. Standard mechanical tests for stents exist (ASTM 2516, F2606, F2394, and F2477), although specialized single-purpose systems are required and not widely available.

Due to the bioresorbable nature of the BRS, degradation affects the stents stiffness, and thus the BRS's ability to preserve an artery open after deployment. A preliminary study was conducted to assess the mechanical properties of degraded HMS. HMS was fabricated using PCL and the composite PCL / EFG 1%, the later composite was chosen based on the mechanical tests for SMS. The addition of EFG had little impact on the degradation profile of HMS. Degradation modifies both the amorphous structure and crystallinity of PC [66]. *In-vivo* degradation of PCL scaffolds was reported between 24% and 48% faster than *in-vitro* hydrolytic degradation [64,80]. Faster degradation may be due to cell-mediated degradation, free radicals, acidic products, biological residues and the presence of different enzymes [80]. Regardless of the degradation method, similar mechanical properties were found in PCL scaffolds matched by weight [64,66,80]. After 6 months of *in-vivo* degradation PCL scaffolds loss only 3% of their mass [64], Enzymatically degrades HMS showed a 40% weight loss after 48 h. Mechanical properties of degraded HMS after 24 h of enzyme exposure may be in the same order of magnitude of those degraded under *in-vivo* conditions. Due to the unique stent architecture and strut dimensions, a different *in-vivo* degradation rate may occur and comparing

these results to published *in-vivo* degradation rates can be difficult. This preliminary study serves to shed light on the structural behavior of degraded HMS fabricated with EFG-composites.

After assessing the mechanical properties of HMS, drug-eluting capabilities were tested. Pcx-loaded HMS fabricated with half of the struts made from PCL and the other half with PCL / EFG 1%. In the PCL group, Pcx was loaded in the PCL struts and in the EFG group, Pcx was loaded into PCL / EFG 1% composite. After 9 days, between 1 and 2% of the Pcx was eluted in the EFG group. In comparison, commercially available Pcx-loaded DES release most of the incorporated drug in the first month after implantation [46]. The cumulative release was slower in the EFG group, albeit no significant differences were found between the same time points. This slower release in the EFG group was due to the modification of the composite hydrophilicity and composite molecular weight by the added nanofiller [19,29,57]. Also, an increase in the molecular weight of the composite carrier can decrease the Pcx release [57]. It remains to be seen if the increase in EFG-nanofiller can significantly modify the drug-eluting profile of PCL. Also, EFG and EFG-TEA composites required future work to measure hydrophilicity and optimize composite preparation. These characteristics were not assessed in this work due to time constraints.

With the use of the Hystent printer, stents can be fabricated with a precise combination of structural support and tailored drug-eluting capabilities. Also, drug-eluting materials with distinct release profiles can be spatially distributed along the stent to provide a customized drug-eluting platform. A prolonged drug-release study is needed to examine the impact in drug-release amongst the rest of the graphene-based composites tested in this research.

5. Conclusion

In this work, the feasibility of developing a customized hybrid-material stent printer, and subsequently 3D printing polymer-based stents was demonstrated. The proposed machine moves one step closer to a one-click solution to produce bioresorbable stents at the doctors' office, in minutes, no post-processing required. Stents were fabricated rapidly and consistently, architectures were tailor-made using a custom G-code generator, this G-code generator can be optimized for different architectures according to the intended application (Figure 5.1). Fabrication of bioresorbable stents with improved mechanical properties using graphene-based composites was achieved. SMS printed using EFG-based composites showed an improvement in mechanical strength and a decreased drug-eluting rate compared to blank PCL without hindering its biodegradable profile. Dynamic feed rate compensation resolved the challenges faced during HMS printing. Nonetheless, the fabrication of HMS requires further optimization in future work.

Figure 5.1. Range of stents and architecture produced in this research project.

Production of hybrid-material stents is feasible, different stent architectures can be obtained using our G-code generator (Fig. 5.1), The use of graphene-based composites for reabsorbable stents with improved mechanical profile was demonstrated. The mechanical performance of hybrid-material stents requires further optimization.

In conclusion:

- Production of hybrid-material stents was found to be feasible;
- Different stent architectures were 3D printed using our G-code generator (Fig. 5.1);
- The use of graphene-based composites for reabsorbable stents with improved mechanical profile was demonstrated;
- Mechanical performance of hybrid-material stents requires further optimization.

6. Future recommendations

Towards a printed BRS using bioresorbable materials, efforts must focus on printing technologies to produce struts thinner than 200 µm with improved mechanical properties. Extrusion based platforms require higher working pressures to consistently print thinner strands, migration to mechanical extrusion might the best option. On the materials aspect, the next step should be the migration into stiffer composites based on PLA with the addition of graphene-based nanofillers. EFG-based composites and the nanofiller dispersion within them requires further optimization. Interactions between the different composites at the joint points must be examined beyond DFC. Also, the incorporation of a heated rotary axis might improve adhesion between polymers.

Mechanical properties ought to be measured on standardized mechanical testing systems to acheive more comparable measurements. Further degradation tests must be performed to include PCL controls to get more insight into the degradation dynamics of printed stents. Hydrolytic degradation studies must be conducted to test the different profiles of PCL and graphene-based composites to then be correlated with *in-vivo* conditions. Long term drug release measurements should be obtained to mimic clinical conditions of implanted stents.

Bibliography

[1] Australian Bureau of Statistics, Australia's leading causes of death, 2016, Aust. Bur. Stat. (2018) 3303. http://www.abs.gov.au/ausstats/abs@.nsf/Lookup/by Subject/3303.0~2016~Main Features~Australia's leading causes of death, 2016~3 (accessed June 20, 2018).

[2] Australian Institute of Health and Welfare, Cardiovascular disease: Australian facts 2011, Australian Institute of Health and Welfare, Canberra, 2011. https://www.aihw.gov.au/getmedia/9621f6a8-f076-4e3e-a9c7-dece59ff0d74/12116.pdf.aspx?inline=true (accessed June 20, 2018).

[3] P.A. Heidenreich, J.G. Trogdon, O.A. Khavjou, J. Butler, K. Dracup, M.D. Ezekowitz, E.A. Finkelstein, Y. Hong, S.C. Johnston, A. Khera, D.M. Lloyd-Jones, S.A. Nelson, G. Nichol, D. Orenstein, P.W.F. Wilson, Y.J. Woo, Forecasting the future of cardiovascular disease in the United States: A policy statement from the American Heart Association, Circulation. 123 (2011) 933–944. https://doi.org/10.1161/CIR.0b013e31820a55f5.

[4] J.L. Anderson, D.A. Morrow, Acute Myocardial Infarction, N. Engl. J. Med. 376 (2017) 2053–2064. https://doi.org/10.1056/NEJMra1606915.

[5] B. Stephen, M. Moscucci, Grossman & Baim's cardiac catheterization, angiography, and intervention, 8th ed., Lippincott Williams & Wilkins, 2013.

[6] P. Grimfjärd, S. James, J. Persson, O. Angerås, S. Koul, E. Omerovic, C. Varenhorst, B. Lagerqvist, D. Erlinge, Outcome of percutaneous coronary intervention with the Absorb bioresorbable scaffold: Data from the Swedish Coronary Angiography and Angioplasty Registry (SCAAR), EuroIntervention. 13 (2017) 1304–1311. https://doi.org/10.4244/EIJ-D-17-00458.

[7] D. Stoeckel, C. Bonsignore, S. Duda, A survey of stent designs, Minim. Invasive Ther. Allied Technol. 11 (2002) 137–147. https://doi.org/10.1080/136457002760273340.

[8] A. Schömig, A. Kastrati, H. Mudra, R. Blasini, H. Schühlen, V. Klauss, G. Richardt, F.J. Neumann, Four-year experience with Palmaz-Schatz stenting in coronary angioplasty complicated by dissection with threatened or present vessel closure., Circulation. 90 (1994) 2716–24. https://doi.org/10.1161/01.cir.102.4.371.

[9] G. Mani, M.D. Feldman, D. Patel, C.M. Agrawal, Coronary stents: A materials perspective, Biomaterials. 28 (2007) 1689–1710. https://doi.org/10.1016/j.biomaterials.2006.11.042.

[10] S. Garg, P.W. Serruys, Coronary stents: Current status, J. Am. Coll. Cardiol. 56 (2010). https://doi.org/10.1016/j.jacc.2010.06.007.

[11] W. Khan, S. Farah, A.J. Domb, Drug eluting stents: Developments and current status, J. Control. Release. 161 (2012) 703–712. https://doi.org/10.1016/j.jconrel.2012.02.010.

[12] A. Lupi, G. Gabrio Secco, A. Rognoni, M. Lazzero, R. Fattori, I. Sheiban, A. Sante Bongo, L. Bolognese, P. Agostoni, I. Porto, Meta-analysis of bioabsorbable versus durable polymer drug-eluting stents in 20,005 patients with coronary artery disease: An update, Catheter. Cardiovasc. Interv. 83 (2014). https://doi.org/10.1002/ccd.25416.

[13] E.P. McFadden, E. Stabile, E. Regar, E. Cheneau, A.T.L. Ong, T. Kinnaird, W.O. Suddath, N.J. Weissman, R. Torguson, K.M. Kent, A.D. Pichard, L.F. Satler, R. Waksman, P.W. Serruys, Late thrombosis in drug-eluting coronary stents after discontinuation of antiplatelet therapy, Lancet. 364 (2004) 1519–1521. https://doi.org/10.1016/S0140-6736(04)17275-9.

[14] H. Tamai, Biodegradable Stents, (2000) 371–373.

[15] Y. Zhu, K. Yang, R. Cheng, Y. Xiang, T. Yuan, B. Sarmento, Y. Cheng, W. Cui, The current status of biodegradable stent to treat benign luminal disease, Mater. Today. 20 (2017) 516–529. https://doi.org/10.1016/j.mattod.2017.05.002.

[16] J.A. Ormiston, P.W.S. Serruys, Bioabsorbable coronary stents, Circ. Cardiovasc. Interv. 2 (2009) 255–260. https://doi.org/10.1161/CIRCINTERVENTIONS.109.859173.

[17] S.H. Im, Y. Jung, S.H. Kim, Current status and future direction of biodegradable metallic and polymeric vascular scaffolds for next-generation stents, Acta Biomater. 60 (2017) 3–22. https://doi.org/10.1016/j.actbio.2017.07.019.

[18] S.-S.D.S.D. Carter, P.F. Costa, C. Vaquette, S. Ivanovski, D.W. Hutmacher, J. Malda, Additive Biomanufacturing: An Advanced Approach for Periodontal Tissue Regeneration, Ann. Biomed. Eng. (2016) 1–11. https://doi.org/10.1007/s10439-016-1687-2.

[19] S.K. Misra, F. Ostadhossein, R. Babu, J. Kus, D. Tankasala, A. Sutrisno, K.A. Walsh, C.R. Bromfield, D. Pan, 3D-Printed Multidrug-Eluting Stent from Graphene-Nanoplatelet-Doped Biodegradable Polymer Composite,

Adv. Healthc. Mater. 6 (2017) 1–14. https://doi.org/10.1002/adhm.201700008.

[20] A. Guerra, A. Roca, J. de Ciurana, A novel 3D additive manufacturing machine to biodegradable stents, Procedia Manuf. 13 (2017) 718–723. https://doi.org/10.1016/j.promfg.2017.09.118.

[21] T. Jungst, M.L. Muerza-Cascante, T.D. Brown, M. Standfest, D.W. Hutmacher, J. Groll, P.D. Dalton, Melt electrospinning onto cylinders: Effects of rotational velocity and collector diameter on morphology of tubular structures, Polym. Int. 64 (2015) 1086–1095. https://doi.org/10.1002/pi.4948.

[22] E. McColl, J. Groll, T. Jungst, P.D. Dalton, Design and fabrication of melt electrowritten tubes using intuitive software, Mater. Des. 155 (2018) 46–58. https://doi.org/10.1016/j.matdes.2018.05.036.

[23] C.S. Lim, P. Eng, S.C. Lin, C.K. Chua, Y.T. Lee, Rapid Prototyping and Tooling of Custom-Made Tracheobronchial Stents, 2002. https://link-springer-com.proxy.library.uu.nl/content/pdf/10.1007%2Fs001700200122.pdf (accessed July 31, 2018).

[24] S.S. Moore, K.J. O'Sullivan, F. Verdecchia, Shrinking the Supply Chain for Implantable Coronary Stent Devices, Ann. Biomed. Eng. 44 (2016) 497–507. https://doi.org/10.1007/s10439-015-1471-8.

[25] L. Freitag, M. Gördes, P. Zarogoulidis, K. Darwiche, D. Franzen, F. Funke, W. Hohenforst-Schmidt, H. Dutau, Towards Individualized Tracheobronchial Stents: Technical, Practical and Legal Considerations, Respiration. 94 (2017) 442–456. https://doi.org/10.1159/000479164.

[26] A.J. Guerra, J. San, J. Ciurana, Fabrication of PCL/PLA Composite Tube for Stent Manufacturing, Procedia CIRP. 65 (2017) 231–235. https://doi.org/10.1016/j.procir.2017.03.339.

[27] D. Vondrys, M.J. Elliott, C.A. McLaren, C. Noctor, D.J. Roebuck, First experience with biodegradable airway stents in children, Ann. Thorac. Surg. 92 (2011) 1870–1874. https://doi.org/10.1016/j.athoracsur.2011.07.042.

[28] Abbott, Absorb Gt1 ™ Bioresorbable Vascular Scaffold System, 2016.

[29] S.H. Kang, I.H. Chae, J.J. Park, H.S. Lee, D.Y. Kang, S.S. Hwang, T.J. Youn, H.S. Kim, Stent Thrombosis With Drug-Eluting Stents and Bioresorbable Scaffolds: Evidence From a Network Meta-Analysis of 147 Trials, JACC Cardiovasc. Interv. 9 (2016) 1203–1212. https://doi.org/10.1016/j.jcin.2016.03.038.

[30] C. Esposito Corcione, F. Gervaso, F. Scalera, F. Montagna, A. Sannino, A. Maffezzoli, The feasibility of printing

polylactic acid–nanohydroxyapatite composites using a low-cost fused deposition modeling 3D printer, J. Appl. Polym. Sci. 134 (2017) 1–10. https://doi.org/10.1002/app.44656.

[31] S. Sayyar, D.L. Officer, G.G. Wallace, Fabrication of 3D structures from graphene-based biocomposites, J. Mater. Chem. B. 5 (2017) 3462–3482. https://doi.org/10.1039/C6TB02442D.

[32] L. Kong, W. Liu, G. Yan, Q. Li, H. Yang, F. Yu, H. Song, Poly-l-lactic acid/amorphous calcium phosphate bioabsorbable stent causes less inflammation than poly-l-lactic acid stent in coronary arteries, Int J Clim Exp Med. 7 (2014) 5317–5323.

[33] J.R. Potts, D.R. Dreyer, C.W. Bielawski, R.S. Ruoff, Graphene-based polymer nanocomposites, Polymer (Guildf). 52 (2011) 5–25. https://doi.org/10.1016/j.polymer.2010.11.042.

[34] M.A. Worsley, P.J. Pauzauskie, T.Y. Olson, J. Biener, J.H. Satcher, T.F. Baumann, Synthesis of Graphene Aerogel with High Electrical Conductivity, (n.d.). https://doi.org/10.1021/ja1072299.

[35] P.C. Sherrell, B.C. Thompson, J.K. Wassei, A.A. Gelmi, M.J. Higgins, R.B. Kaner, G.G. Wallace, Maintaining cytocompatibility of biopolymers through a graphene layer for electrical stimulation of nerve cells, Adv. Funct. Mater. 24 (2014) 769–776. https://doi.org/10.1002/adfm.201301760.

[36] S. Sayyar, R. Cornock, E. Murray, S. Beirne, D.L. Officer, G.G. Wallace, Extrusion Printed Graphene/Polycaprolactone/Composites for Tissue Engineering, Mater. Sci. Forum. 773–774 (2013) 496–502. https://doi.org/10.4028/www.scientific.net/MSF.773-774.496.

[37] F. Ordikhani, M.R. Farani, M. Dehghani, E. Tamjid, A. Simchi, Physicochemical and biological properties of electrodeposited graphene oxide/chitosan films with drug-eluting capacity, Carbon N. Y. 84 (2015) 91–102. https://doi.org/10.1016/j.carbon.2014.11.052.

[38] K. Yang, S. Zhang, G. Zhang, X. Sun, S.-T. Lee, Z. Liu, Graphene in Mice: Ultrahigh In Vivo Tumor Uptake and Efficient Photothermal Therapy, (n.d.). https://doi.org/10.1021/nl100996u.

[39] S. McMahon, N. Bertollo, E.D.O. Cearbhaill, J. Salber, L. Pierucci, P. Duffy, T. Dürig, V. Bi, W. Wang, Bio-resorbable polymer stents: a review of material progress and prospects, Prog. Polym. Sci. 83 (2018) 79–96. https://doi.org/10.1016/j.progpolymsci.2018.05.002.

[40] E.J. Chung, H.W. Ju, H.J. Park, C.H. Park, Three-layered scaffolds for artificial esophagus using

poly(caprolactone) nanofibers and silk fibroin: An experimental study in a rat model, J. Biomed. Mater. Res. - Part A. 103 (2015) 2057–2065. https://doi.org/10.1002/jbm.a.35347.

[41] X. Yu, T. Takayama, S.A. Goel, X. Shi, Y. Zhou, K.C. Kent, W.L. Murphy, L.W. Guo, A rapamycin-releasing perivascular polymeric sheath produces highly effective inhibition of intimal hyperplasia, J. Control. Release. 191 (2014) 47–53. https://doi.org/10.1016/j.jconrel.2014.05.017.

[42] N. Foin, R.D. Lee, R. Torii, J.L. Guitierrez-Chico, A. Mattesini, S. Nijjer, S. Sen, R. Petraco, J.E. Davies, C. Di Mario, M. Joner, R. Virmani, P. Wong, Impact of stent strut design in metallic stents and biodegradable scaffolds, Int. J. Cardiol. 177 (2014) 800–808. https://doi.org/10.1016/j.ijcard.2014.09.143.

[43] W. Schmidt, P. Behrens, C. Brandt-Wunderlich, S. Siewert, N. Grabow, K.P. Schmitz, In vitro performance investigation of bioresorbable scaffolds – Standard tests for vascular stents and beyond, Cardiovasc. Revascularization Med. 17 (2016) 375–383. https://doi.org/10.1016/j.carrev.2016.05.001.

[44] J.F. Dyet, W.G. Watts, D.F. Ettles, A.A. Nicholson, Mechanical properties of metallic stents: How do these properties influence the choice of stent for specific lesions?, Cardiovasc. Intervent. Radiol. 23 (2000) 47–54. https://doi.org/10.1007/s002709910007.

[45] S. Beier, J. Ormiston, M. Webster, J. Cater, S. Norris, P. Medrano-Gracia, A. Young, B. Cowan, Hemodynamics in Idealized Stented Coronary Arteries: Important Stent Design Considerations, Ann. Biomed. Eng. 44 (2016) 315–329. https://doi.org/10.1007/s10439-015-1387-3.

[46] Y. Huang, H.C.A. Ng, X.W. Ng, V. Subbu, Drug-eluting biostable and erodible stents, J. Control. Release. 193 (2014) 188–201. https://doi.org/10.1016/j.jconrel.2014.05.011 Review.

[47] L. Laboratories, Safety Data Sheet - Paclitaxel, 2018.

[48] E. Grube, L. Bullesfeld, Initial Experience with Paclitaxel-Coated Stents, (n.d.). https://onlinelibrary-wiley-com.proxy.library.uu.nl/doi/pdf/10.1111/j.1540-8183.2002.tb01091.x (accessed June 24, 2018).

[49] A. V. Finn, G. Nakazawa, M. Joner, F.D. Kolodgie, E.K. Mont, H.K. Gold, R. Virmani, Vascular responses to drug eluting stents: Importance of delayed healing, Arterioscler. Thromb. Vasc. Biol. 27 (2007) 1500–1510. https://doi.org/10.1161/ATVBAHA.107.144220.

[50] E. TDK, NTC thermistors for temperature measurement Probe assemblies, TDK, 2009.

[51] S. Sayyar, E. Murray, B.C. Thompson, S. Gambhir, D.L. Officer, G.G. Wallace, Covalently linked biocompatible graphene/polycaprolactone composites for tissue engineering, Carbon N. Y. 52 (2013) 296–304. https://doi.org/10.1016/j.carbon.2012.09.031.

[52] D. Dollimore, P. Phang, Thermal Analysis, Anal. Chem. 72 (2000) 27–36. https://doi.org/10.1021/a1000003j.

[53] M.N. Brodmerkel, P.G.G. Wallace, P.P. Dalton, 3D printed degradable stents with controlled drug delivery capabilities, (n.d.).

[54] S.C. Kim, J. Yu, J.W. Lee, E.-S. Park, S.-C. Chi, Sensitive HPLC method for quantitation of paclitaxel (Genexol ®) in biological samples with application to preclinical pharmacokinetics and biodistribution, J. Pharm. Biomed. Anal. 39 (2005) 170–176. https://doi.org/10.1016/j.jpba.2005.02.023.

[55] E. Murray, B.C. Thompson, S. Sayyar, G.G. Wallace, Enzymatic degradation of graphene / polycaprolactone materials for tissue engineering, Polym. Degrad. Stab. 111 (2015) 71–77. https://doi.org/10.1016/j.polymdegradstab.2014.10.010.

[56] F. He, S. Li, M. Vert, R. Zhuo, Enzyme-catalyzed polymerization and degradation of copolymers prepared from ϵ-caprolactone and poly(ethylene glycol), Polymer (Guildf). 44 (2003) 5145–5151. https://doi.org/10.1016/S0032-3861(03)00562-7.

[57] A. Angelopoulou, E. Voulgari, E.K. Diamanti, D. Gournis, K. Avgoustakis, Graphene oxide stabilized by PLA-PEG copolymers for the controlled delivery of paclitaxel, Eur. J. Pharm. Biopharm. 93 (2015) 18–26. https://doi.org/10.1016/j.ejpb.2015.03.022.

[58] M.J. Jenkins, K.L. Harrison, The effect of molecular weight on the crystallization kinetics of polycaprolactone, Polym. Adv. Technol. 17 (2006) 474–478. https://doi.org/10.1002/pat.733.

[59] C. Corcione, M. Frigione, Characterization of Nanocomposites by Thermal Analysis, Materials (Basel). 5 (2012) 2960–2980. https://doi.org/10.3390/ma5122960.

[60] R.H. Colby, D.C. Boris, W.E. Krause, S. Dou, Shear thinning of unentangled flexible polymer liquids, Rheol. Acta. 46 (2007) 569–575. https://doi.org/10.1007/s00397-006-0142-y.

[61] X. Huang, Z. Yin, S. Wu, X. Qi, Q. He, Q. Zhang, Q. Yan, F. Boey, H. Zhang, Graphene-Based Materials: Synthesis, Characterization, Properties, and Applications, Small. 7 (2011) 1876–1902.

https://doi.org/10.1002/smll.201002009.

[62] A.C. Ferrari, J. Robertson, Interpretation of Raman spectra of disordered and amorphous carbon, Phys. Rev. B. 61 (2000) 14095–14107. https://doi.org/10.1007/BF02543692.

[63] B. Tang, H. Guoxin, H. Gao, Raman spectroscopic characterization of graphene, Appl. Spectrosc. Rev. 45 (2010) 369–407. https://doi.org/10.1080/05704928.2010.483886.

[64] C.X.F. Lam, D.W. Hutmacher, J.-T. Schantz, M.A. Woodruff, S.H. Teoh, Evaluation of polycaprolactone scaffold degradation for 6 months *in vitro* and *in vivo*, J. Biomed. Mater. Res. Part A. 90A (2009) 906–919. https://doi.org/10.1002/jbm.a.32052.

[65] G. Acharya, K. Park, Mechanisms of controlled drug release from drug-eluting stents, Adv. Drug Deliv. Rev. 58 (2006) 387–401. https://doi.org/10.1016/j.addr.2006.01.016.

[66] I. Castilla-Cortázar, J. Más-Estellés, J.M. Meseguer-Dueñas, J.L. Escobar Ivirico, B. Marí, A. Vidaurre, Hydrolytic and enzymatic degradation of a poly(ε-caprolactone) network, Polym. Degrad. Stab. 97 (2012) 1241–1248. https://doi.org/10.1016/j.polymdegradstab.2012.05.038.

[67] T.S. Renuga Devi, S. Gayathri, FTIR And FT-Raman spectral analysis of Paclitaxel drugs, Int. J. Pharm. Sci. Rev. Res. 2 (2010) 106–110. http://global-research-online.net/journalcontents/volume2issue2/Article 019.pdf (accessed June 26, 2018).

[68] H. Salehi, E. Middendorp, I. Panayotov, P.-Y.C. Dutilleul, A.-G. Vegh, S. Ramakrishnan, C. Gergely, F. Cuisinier, Confocal Raman data analysis enables identifying apoptosis of MCF-7 cells caused by anticancer drug paclitaxel, J. Biomed. Opt. 18 (2013) 056010. https://doi.org/10.1117/1.JBO.18.5.056010.

[69] A. Eckmann, A. Felten, A. Mishchenko, L. Britnell, R. Krupke, K.S. Novoselov, C. Casiraghi, Probing the nature of defects in graphene by Raman spectroscopy, Nano Lett. 12 (2012) 3925–3930. https://doi.org/10.1021/nl300901a.

[70] M.A. Pimenta, G. Dresselhaus, M.S. Dresselhaus, L.G. Cançado, A. Jorio, R. Saito, Studying disorder in graphite-based systems by Raman spectroscopy, Phys. Chem. Chem. Phys. 9 (2007) 1276–1291. https://doi.org/10.1039/b613962k.

[71] P. Bhawal, S. Ganguly, T.K. Chaki, N.C. Das, Synthesis and characterization of graphene oxide filled ethylene

methyl acrylate hybrid nanocomposites, RSC Adv. 6 (2016) 20781–20790. https://doi.org/10.1039/C5RA24914G.

[72] A.J. Guerra, J. Ciurana, 3D-printed bioabsordable polycaprolactone stent: The effect of process parameters on its physical features, Mater. Des. 137 (2018) 430–437. https://doi.org/10.1016/j.matdes.2017.10.045.

[73] C.M. Valmikinathan, J. Tian, J. Wang, X. Yu, Novel nanofibrous spiral scaffolds for neural tissue engineering, J. Neural Eng. 5 (2008) 422–432. https://doi.org/10.1088/1741-2560/5/4/007.

[74] K. Bilodeau, F. Couet, F. Boccafoschi, D. Mantovani, Design of a Perfusion Bioreactor Specific to the Regeneration of Vascular Tissues Under Mechanical Stresses, Artif. Organs. 29 (2005) 906–912. https://doi.org/10.1111/j.1525-1594.2005.00154.x.

[75] R.E. De Filippo, B.S. Kornitzer, J.J. Yoo, A. Atala, Penile urethra replacement with autologous cell-seeded tubularized collagen matrices, J. Tissue Eng. Regen. Med. 9 (2015) 257–264. https://doi.org/10.1002/term.1647.

[76] P. Song, Z. Cao, Y. Cai, L. Zhao, Z. Fang, S. Fu, Fabrication of exfoliated graphene-based polypropylene nanocomposites with enhanced mechanical and thermal properties, Polymer (Guildf). 52 (2011) 4001–4010. https://doi.org/10.1016/j.polymer.2011.06.045.

[77] L.-C. Tang, Y.-J. Wan, D. Yan, Y.-B. Pei, L. Zhao, Y.-B. Li, L.-B. Wu, J.-X. Jiang, G.-Q. Lai, The effect of graphene dispersion on the mechanical properties of graphene/epoxy composites, Carbon N. Y. 60 (2013) 16–27. https://doi.org/10.1016/j.carbon.2013.03.050.

[78] R. Hashemi Sanatgar, C. Campagne, V. Nierstrasz, Investigation of the adhesion properties of direct 3D printing of polymers and nanocomposites on textiles: Effect of FDM printing process parameters, Appl. Surf. Sci. 403 (2017) 551–563. https://doi.org/10.1016/j.apsusc.2017.01.112.

[79] A. Karimi, M. Navidbakhsh, A. Shojaei, S. Faghihi, Measurement of the uniaxial mechanical properties of healthy and atherosclerotic human coronary arteries, Mater. Sci. Eng. C. 33 (2013) 2550–2554. https://doi.org/10.1016/j.msec.2013.02.016.

[80] N. Bölgen, Y.Z. Menceloğlu, K. Acatay, I. Vargel, E. Pişkin, In vitro and in vivo degradation of non-woven materials made of poly(epsilon-caprolactone) nanofibers prepared by electrospinning under different

conditions., J. Biomater. Sci. Polym. Ed. 16 (2005) 1537–1555. https://doi.org/10.1163/156856205774576655.

Appendix A

Schematics of the 3D printed clamp adaptor used for mechanical testing.

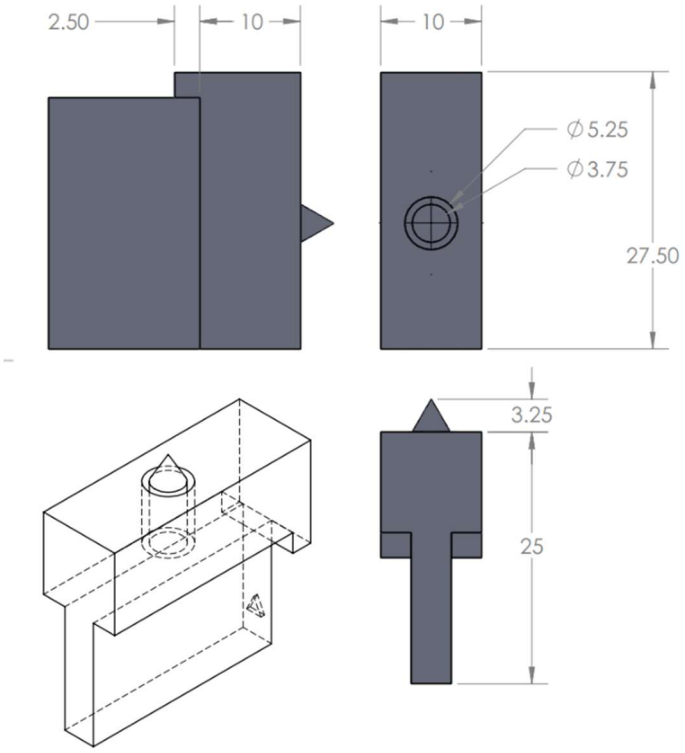

Clamp adaptor used for stent mechanical testing. Scales in mm.

Appendix B

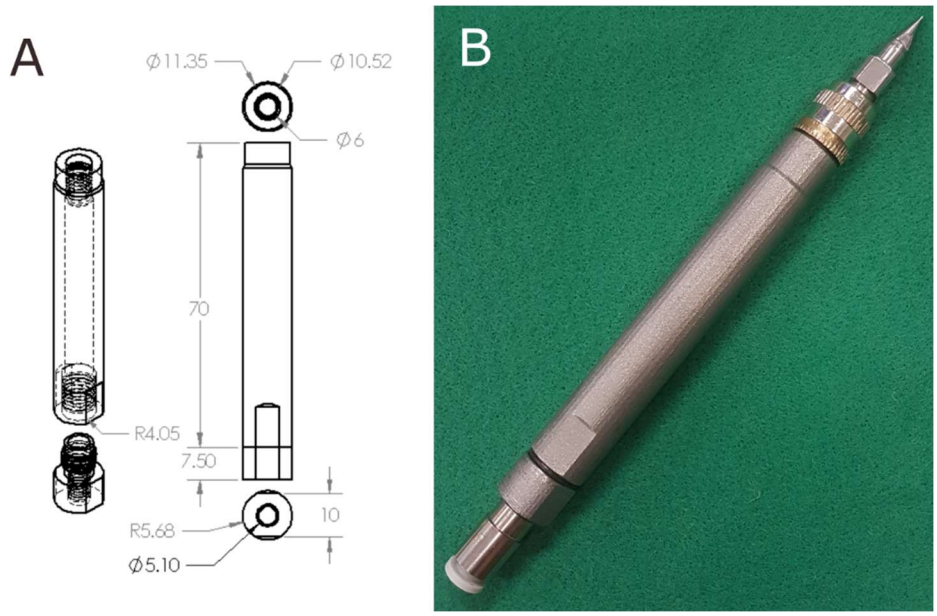

3D-printed titanium cartridges. A, CAD design. B, printed version. This customized cartridge can be pressurized up to 1 MPa. It was designed compatible with current laboratory equipment and easy to clean, including the nozzle that can be disassembled for a thorough cleaning.

Appendix C

Macro use in TA Instruments Universal Analysis software to analyze TGA curves. This macro obtains the degradation temperature and the temperature at 10% weight loss.

Program: Universal Analysis V4.5A

Macro: Decomp/T0.1

Steps: 8

Created: 12-Jul-2018 13:27:34

Revised: 12-Jul-2018 13:41:01

1: Function Glass/Step Transition

2: Cursor Point 1 (200.0, 99.7901)

3: Cursor Point 2 (500.0, 4.64198)

4: Function Accept Cursor Limits

5: Button OK Transition Label

6: Function Temperature at Weight %

7: Cursor Point 1 (374.998, 90.0)

8: Function Accept Cursor Limits

Appendix D

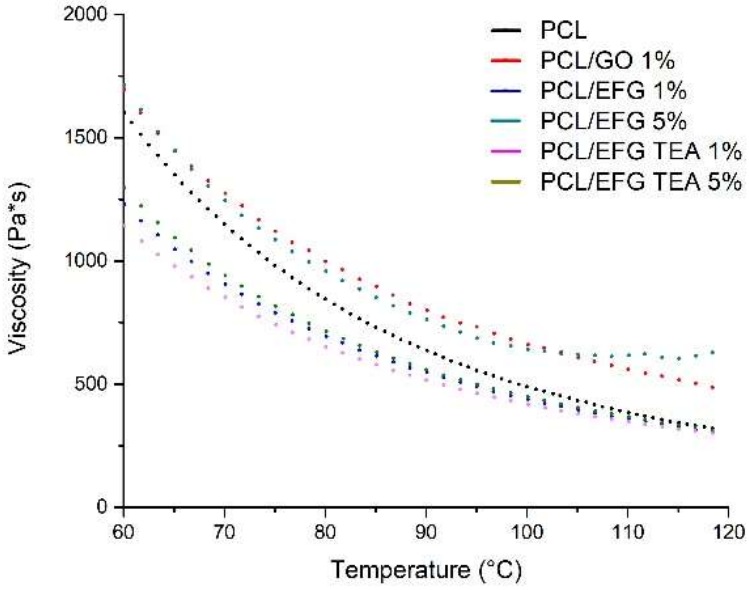

Viscosity curves of PCL and PCL / graphene-based composites vs temperature. Composites were tested at a constant share rate of 1/s.

Appendix E

Standard calibration was made using Pcx diluted in a solution comprised of 55% milliQ water and 45% CH_3CN. Pcx concentration ranged from 10 to 0.125 mg/µL. The limit of detection was defined as the lowest concentration of Pcx resulting in a clear peak greater than the background noise. High detection accuracy was measured as linearity of 0.99466.

Paclitaxel at exp. RT: 8.493

VWD1 A, Wavelength=230 nm

Correlation: 0.99466

Residual Std. Dev.: 57.83086

Formula: y = mx + b

m: 19.70858

b: 2.38317e-1

x: Amount

y: Area

Calibration level weights	
Level 1	1
Level 2	0.5
Level 3	0.255102
Level 4	0.127551
Level 5	0.064103
Level 6	0.032051
Level 7	0.016026
Level 8	0.008013
Level 9	0.004
Level 10	0.002
Level 11	0.001
Level 12	0.0005
Level 13	0.00025
Level 14	0.000125

.

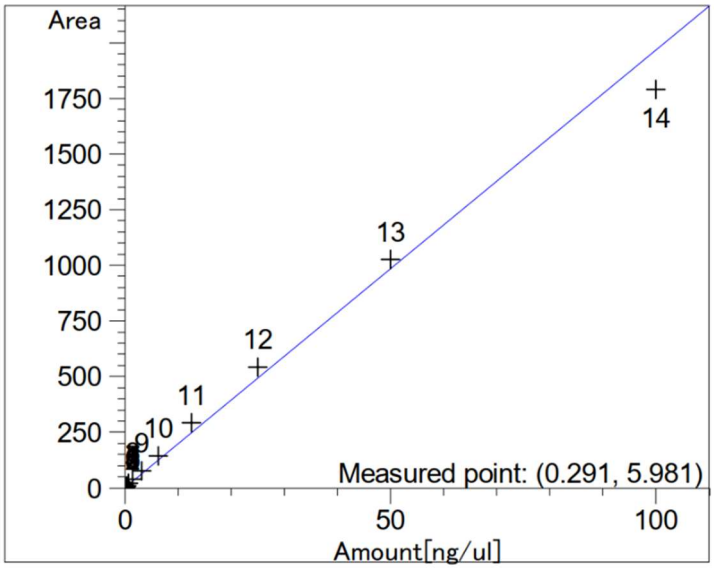

Appendix F

SEM imaging of cross-sectional of graphene-based composite fibers. Samples were frozen in liquid nitrogen and fractured. Then, a 15nm platinum coating was applied. Magnification 500x (left) and 2500x (right). A more uniform distribution can be seen in the composites with GO, EFG 5% and EFG TEA 1%. Composite manufacture optimization was beyond the scope of this research.

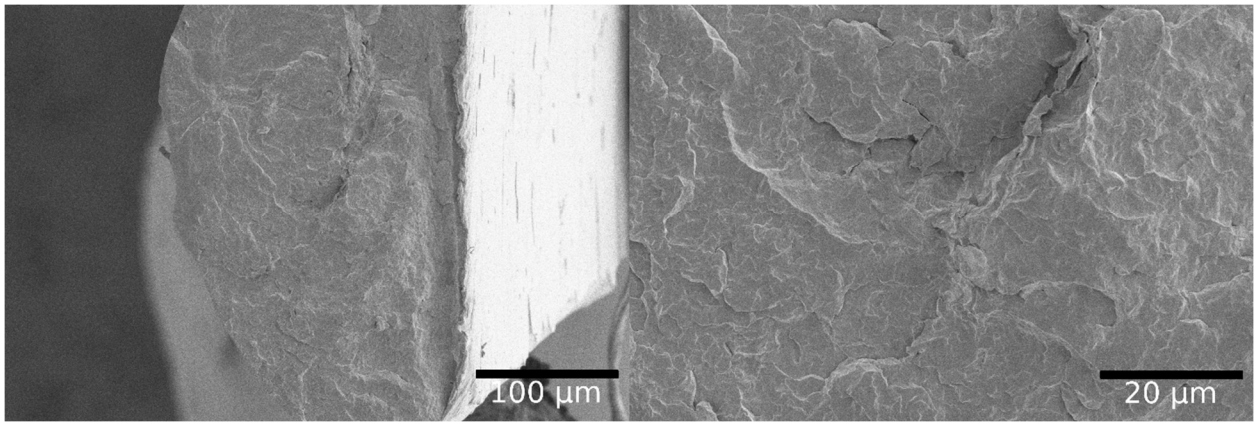

PCL / GO 1%

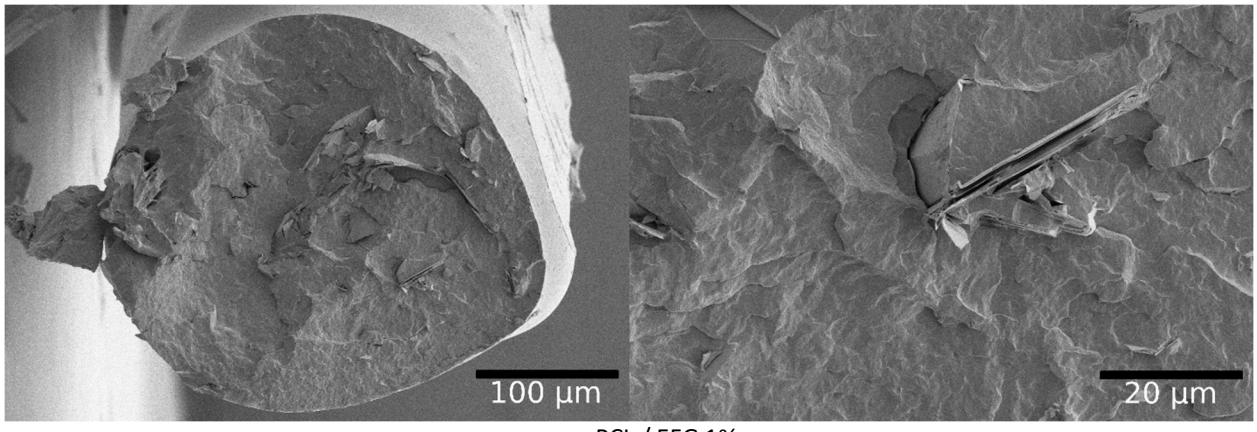

PCL / EFG 1%

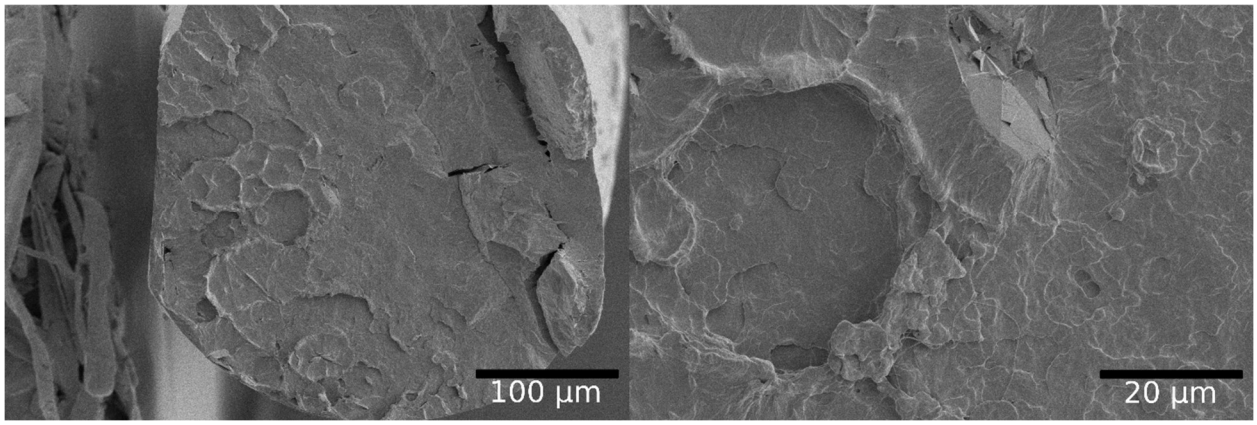

PCL / EFG 5%

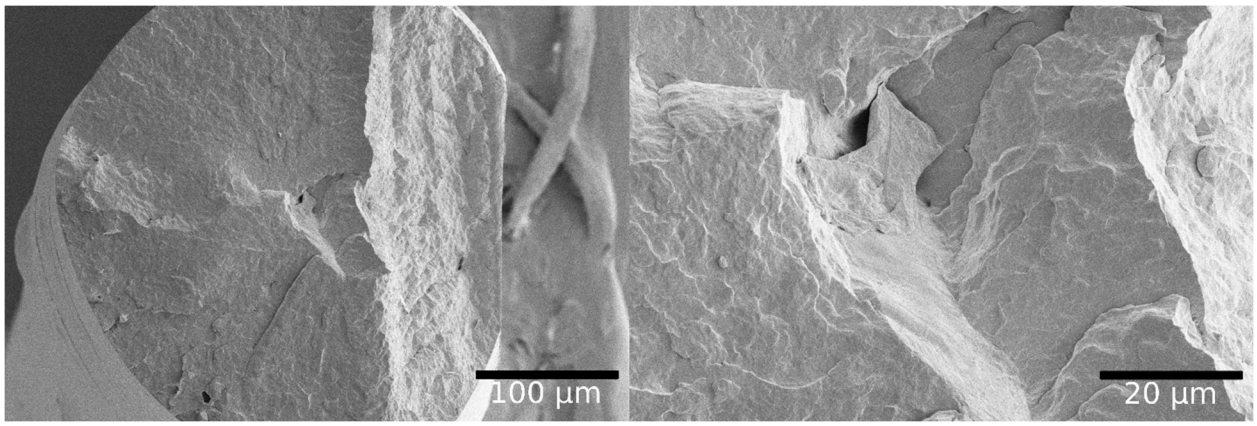

PCL / EFG TEA 1%

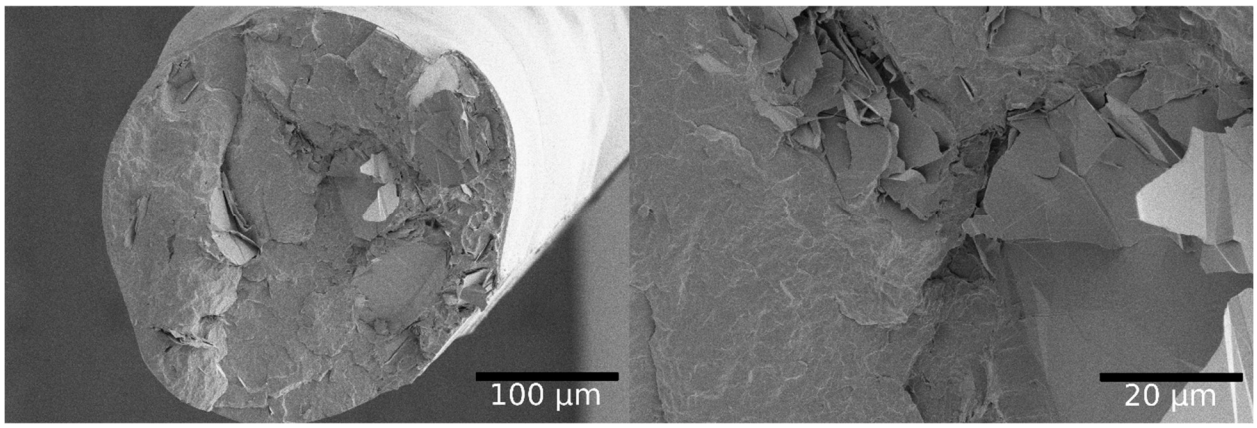

PCL / EFG TEA 5%